Published OnlineFirst May 6, 2020; DOI: 10.1158/2159-8290.CD-19-1242

RESEARCH ARTICLE

Somatic Tissue Engineering in Mouse Models Reveals an Actionable Role for WNT Pathway Alterations in Prostate Cancer Metastasis

Josef Leibold[1], Marcus Ruscetti[1], Zhen Cao[2,3], Yu-Jui Ho[1], Timour Baslan[1], Min Zou[4], Wassim Abida[5], Judith Feucht[6], Teng Han[3,7], Francisco M. Barriga[1], Kaloyan M. Tsanov[1], Leah Zamechek[1], Amanda Kulick[8], Corina Amor[1], Sha Tian[1], Katarzyna Rybczyk[1], Nelson R. Salgado[1], Francisco J. Sánchez-Rivera[1], Philip A. Watson[2], Elisa de Stanchina[8], John E. Wilkinson[9], Lukas E. Dow[7], Cory Abate-Shen[4], Charles L. Sawyers[2,10], and Scott W. Lowe[1,10]

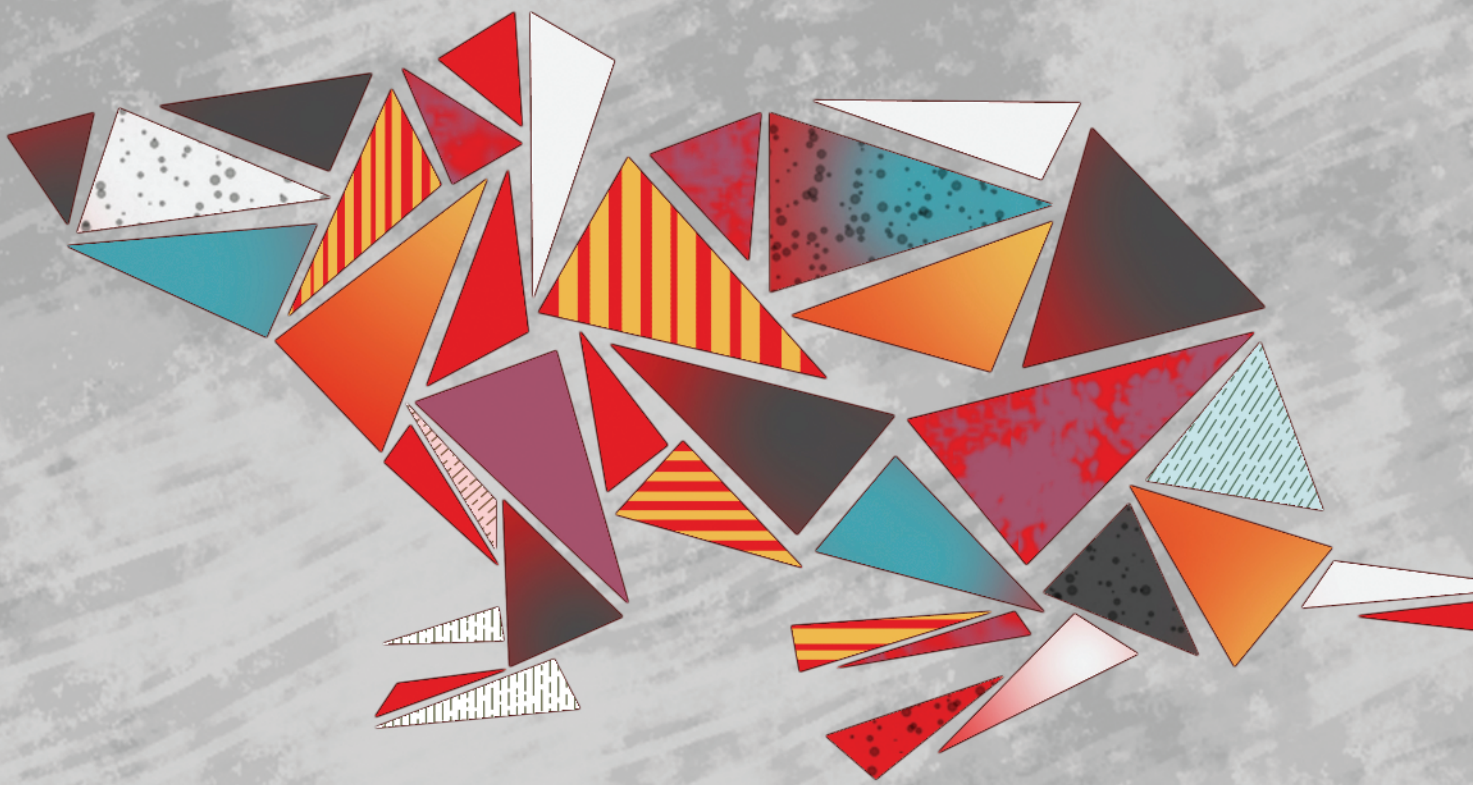

Published OnlineFirst May 6, 2020; DOI: 10.1158/2159-8290.CD-19-1242

ABSTRACT To study genetic factors influencing the progression and therapeutic responses of advanced prostate cancer, we developed a fast and flexible system that introduces genetic alterations relevant to human disease directly into the prostate glands of mice using tissue electroporation. These electroporation-based genetically engineered mouse models (EPO-GEMM) recapitulate features of traditional germline models and, by modeling genetic factors linked to late-stage human disease, can produce tumors that are metastatic and castration-resistant. A subset of tumors with *Trp53* alterations acquired spontaneous WNT pathway alterations, which are also associated with metastatic prostate cancer in humans. Using the EPO-GEMM approach and an orthogonal organoid-based model, we show that WNT pathway activation drives metastatic disease that is sensitive to pharmacologic WNT pathway inhibition. Thus, by leveraging EPO-GEMMs, we reveal a functional role for WNT signaling in driving prostate cancer metastasis and validate the WNT pathway as therapeutic target in metastatic prostate cancer.

SIGNIFICANCE: Our understanding of the factors driving metastatic prostate cancer is limited by the paucity of models of late-stage disease. Here, we develop EPO-GEMMs of prostate cancer and use them to identify and validate the WNT pathway as an actionable driver of aggressive metastatic disease.

INTRODUCTION

Prostate cancer is the most frequent cancer in American men and the second leading cause of their cancer-associated death (1). Although localized disease is associated with an excellent prognosis, the 5-year survival rate drops dramatically in patients with metastatic prostate cancer, from nearly 100% to 30%. Androgen deprivation therapy (ADT) has been the therapy of choice for patients with prostate cancer for several decades (2); however, many patients who initially respond acquire resistance to ADT and eventually develop metastatic castration-resistant prostate cancer (mCRPC).

Advanced prostate cancer is extensively characterized on the molecular level. In addition to androgen receptor (AR) amplification and activation of other AR pathway genes that are induced to bypass ADT, recent sequencing studies have identified various "noncanonical drivers" such as loss of *TP53*, amplification of *MYC* and *MYCN*, and alterations in the PI3K, WNT, and/or DNA repair pathways to be enriched in advanced prostate cancer (3–8). Yet, the potential functional role of many of these genetic alterations in driving either castration resistance or metastasis is unclear.

One way to study the functional role of various genetic perturbations in a physiologic context is through the use of genetically engineered mouse models (GEMM). Although these models have been critical for our understanding of prostate cancer biology as well as for preclinical testing of new therapies (9), they lack the flexibility to test the impact of potential genetic drivers in a timely manner. GEMMs of prostate cancer have additional limitations: (i) many common genotypes are not represented; (ii) most prostate-specific promoters used are androgen dependent, making the study of androgen deprivation in these models difficult; (iii) extensive intercrossing is needed to produce the alleles required for lethal disease; (iv) tumor latency is long; (v) metastatic penetrance is often low; and (vi) genes are frequently altered throughout the tissue, leading to multifocal tumors and potential effects of gene mutations on normal tissue that are not reflective of the human scenario.

In an effort to overcome these limitations, we took advantage of *in vivo* tissue electroporation (10–13) to produce somatic alterations directly in the prostate gland of otherwise wild-type (WT) mice. We envisioned that this approach would produce focal prostate tumors of defined cancer genotypes, enabling the assessment of disease progression and/or therapy response in a physiologic context in both a cost- and time-sensitive manner compared with that required for the production of multiallelic germline strains. After validating the method in comparison with traditional GEMMs, we then used

[1]Department of Cancer Biology and Genetics, Memorial Sloan Kettering Cancer Center, New York, New York. [2]Human Oncology and Pathogenesis Program, Memorial Sloan Kettering Cancer Center, New York, New York. [3]Weill Cornell Graduate School of Medical Sciences, Weill Cornell Medicine, New York, New York. [4]Departments of Pharmacology, Urology, Medicine, Pathology and Cell Biology, and Systems Biology, Herbert Irving Comprehensive Cancer Center, Columbia University Medical Center, New York, New York. [5]Department of Medicine, Memorial Sloan Kettering Cancer Center, New York, New York. [6]Center for Cell Engineering and Immunology Program, Memorial Sloan Kettering Cancer Center, New York, New York. [7]Sandra and Edward Meyer Cancer Center, Department of Medicine, Weill Cornell Medicine, New York, New York. [8]Department of Molecular Pharmacology, Memorial Sloan Kettering Cancer Center, New York, New York. [9]Department of Pathology, University of Michigan, Ann Arbor, Michigan. [10]Howard Hughes Medical Institute, Chevy Chase, Maryland.

Note: Supplementary data for this article are available at Cancer Discovery Online (http://cancerdiscovery.aacrjournals.org/).

J. Leibold, M. Ruscetti, and Z. Cao contributed equally to this work.

Corresponding Authors: Scott W. Lowe, Memorial Sloan Kettering Cancer Center, 417 East 68th Street, New York, NY 10065. Phone: 646-888-3342; Fax: 646-888-3347; E-mail: lowes@mskcc.org; and Charles L. Sawyers, Memorial Sloan Kettering Cancer Center, 1275 York Avenue, New York, NY 10065. Phone: 646-888-2138; Fax: 646-888-3407; E-mail: sawyersc@mskcc.org

Cancer Discov 2020;10:1038–57

doi: 10.1158/2159-8290.CD-19-1242

Published OnlineFirst May 6, 2020; DOI: 10.1158/2159-8290.CD-19-1242

the electroporation-based GEMM (EPO-GEMM) approach to study genetic alterations associated with late-stage prostate cancer and confirmed our results with an orthogonal organoid-based approach. These models identify WNT pathway alterations as actionable events that drive prostate cancer metastasis.

RESULTS

Somatic Induction of Oncogenic Lesions by *In Vivo* Electroporation of the Prostate Gland

As a first attempt to produce prostate carcinoma in mice using tissue electroporation, we chose to introduce alterations leading to *MYC* overexpression and PTEN loss, which co-occur in advanced human prostate cancer and have been previously validated as prostate cancer drivers in mice (refs. 14, 15; Supplementary Fig. S1A). To this end, we performed a survival surgery to expose the prostate and delivered a plasmid cocktail containing (i) a transposon vector expressing a human *MYC* cDNA, (ii) a Sleeping Beauty transposase (SB13), and (iii) a gene-editing vector coexpressing Cas9 and a single-guide RNA (sgRNA) targeting *Pten* into one anterior lobe of the prostate of C57BL/6 male mice via *in vivo* electroporation (Fig. 1A). Although introduction of the transposon vector (to overexpress *MYC*) or the CRISPR/Cas9 vector (to edit *Pten*) alone did not produce tumors for up to 1 year after electroporation, the combination was highly oncogenic, with lethal tumors arising with 83% penetrance and producing a median overall survival of 88 days (Fig. 1B).

We compared the resulting tumor features with tumors arising in a classic GEMM model harboring *MYC* overexpression and a conditional *Pten* allele: *Nkx3.1*$^{CreERT2/+}$;*Pten*$^{fl/fl}$;*ARR2/Pbsn-MYC* (*NP*^{hi}*MYC*) mice (Zou and colleagues, in preparation; ref. 14). As was noted in the germline model, *MYC;sgPten* (*MPt*) EPO-GEMM tumors harbored prostatic intraepithelial neoplasia lesions (Supplementary Fig. S1B) together with regions of well-differentiated adenocarcinoma that expressed high levels of the luminal markers AR and Cytokeratin 8 (CK8) and moderate levels of MYC and the proliferation marker Ki-67 (Fig. 1C; Supplementary Fig. S1C and S1D). Concurrently, many lesions contained adjacent poorly differentiated tumor regions with reduced to absent expression of AR and CK8, and a higher frequency of Ki-67 compared with areas of well-differentiated adenocarcinoma (Fig. 1D; Supplementary Fig. S1C and S1D). Occasionally, poorly differentiated areas also expressed the neuroendocrine (NE) marker synaptophysin (SYP; Fig. 1D). As in the germline model, *MPt* EPO-GEMM tumors metastasized to lymph nodes, liver, and lungs (Supplementary Fig. S1E). *NP*^{hi}*MYC* classic GEMM mice develop metastasis with higher penetrance than *MPt* EPO-GEMM mice (>80% vs. 54%), which is likely because of the accelerated rate of disease formation and death in the EPO-GEMM model (median survival >300 vs. 87.5 days; Zou and colleagues, in preparation) as well as differences in the genetic background of the mice. These results validate the EPO-GEMM platform as a fast and feasible system to model lethal, metastatic prostate cancer in mice.

Engineering Advanced Prostate Cancer *De Novo* Using EPO-GEMMs

Alterations in the *TP53* tumor suppressor are rarely seen in early stages of prostate cancer but are among the most frequently altered genes in advanced disease (4, 16), where they portend a particularly poor prognosis (17). *TP53* alterations also frequently co-occur with *MYC* amplifications in patients with prostate cancer (Supplementary Fig. S2A). We therefore tested whether the combination of *MYC* overexpression with *Trp53* (hereafter simply referred to as *p53*) disruption could lead to advanced prostate cancer in the EPO-GEMM platform (Supplementary Fig. S2B). Although delivery of the *MYC*-containing transposon vector or plasmids expressing a *p53* sgRNA and Cas9 (to edit *p53*) alone did not lead to tumor formation up to 1 year after surgery, *MYC;sgp53* (*MP*) mice developed lethal prostate cancer as early as 64 days after electroporation, with 76% penetrance and a median survival of 114 days (Fig. 2A). Macroscopically, primary tumors were identified in the anterior lobe of the prostate, and approximately 64% of the animals showed metastatic spread to the lymph nodes, peritoneum, liver, or lungs (Fig. 2B). Of note, although disseminated tumor cells (DTC) could be detected in the bone marrow using sensitive PCR approaches (Supplementary Fig. S2C), macroscopic bone metastasis was not observed using either histologic or radiographic approaches (data not shown), suggesting that these genetic alterations might primarily lead to metastasis formation in soft tissues.

We next characterized the histologic, biological, and molecular features of *MP* prostate tumors. Both primary tumors and distant metastases consisted of poorly differentiated prostate cancer with low to absent expression of the luminal markers AR and CK8, basal marker Cytokeratin 5 (CK5), and neuroendocrine marker SYP, and high levels of MYC and Ki-67 expression (Fig. 2C; Supplementary Fig. S2D). As *MP* tumors were mostly negative for both AR and neuroendocrine markers (Fig. 2C; Supplementary Fig. S2D–S2F), they resemble "double-negative" prostate cancer (DNPC), a subtype that has recently been described in patients with castration-resistant prostate cancer (CRPC) with increasing frequency and is enriched for alterations in *TP53* (18). Gene set enrichment analysis (GSEA) following RNA sequencing (RNA-seq) revealed that, despite some heterogeneity in AR activity, the majority of *MP* tumors displayed low expression of AR and neuroendocrine transcriptional signatures, consistent with DNPC (refs. 19, 20; Supplementary Fig. S2G). In line with these findings, histologic characterization of a human CRPC patient tumor harboring *MYC* and *TP53* alterations revealed heterogeneous areas that had high expression of the luminal markers AR and CK8 or the neuroendocrine marker SYP, as well as others that showed low to absent expression of both AR and neuroendocrine markers (i.e., DNPC; Supplementary Fig. S2H).

Because the EPO-GEMM approach does not *a priori* discriminate between cell types within a targeted tissue, we set out to confirm that the tumors we observed were derived from the epithelial compartment. One powerful feature of the method is the ability to introduce somatic alterations into hosts of different genetic backgrounds to rapidly enable improved resolution of the target cell or, in principle, the study of tumor–host interactions. In one series of experiments, a plasmid encoding Cre recombinase was electroporated into the anterior prostate lobe of mice containing a Lox-Stop-Lox (LSL)-mKate cassette, and tissues were examined for mKate fluorescence in prostate luminal and basal

Published OnlineFirst May 6, 2020; DOI: 10.1158/2159-8290.CD-19-1242

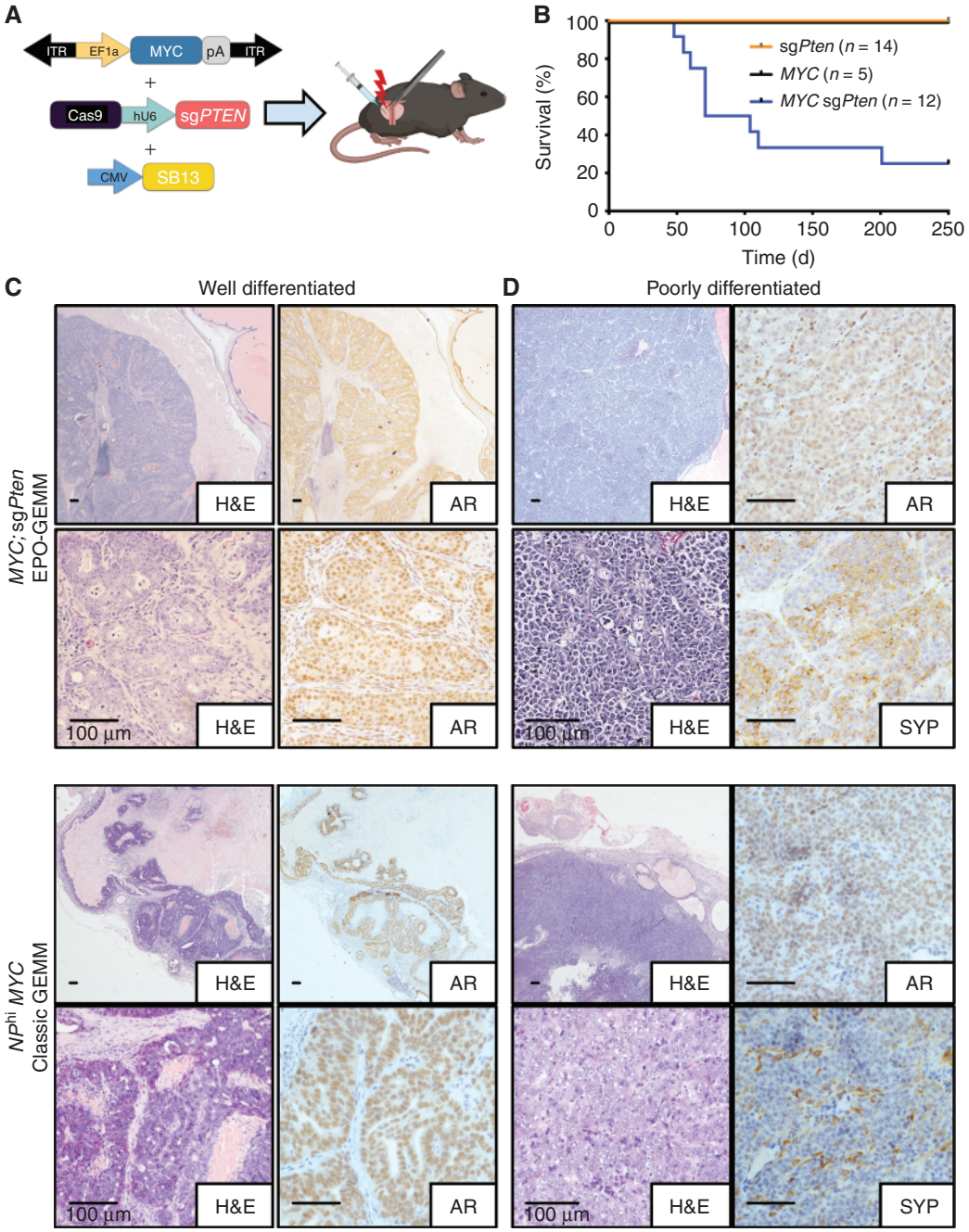

Figure 1. Somatic induction of oncogenic lesions by *in vivo* electroporation of the prostate gland. **A,** Schematic of the EPO-GEMM of prostate cancer. A *MYC* transposon vector in combination with a Sleeping Beauty transposase (SB13) and/or a CRISPR/Cas9 vector targeting *Pten* (sg*Pten*) were delivered into the prostate by direct *in vivo* electroporation. **B,** Kaplan–Meier survival curve of C57BL/6 mice electroporated with a *MYC* transposon vector and a Sleeping Beauty transposase (*MYC*; black), a CRISPR/Cas9 vector targeting *Pten* (sg*Pten*; orange), or the combination of all vectors (*MYC* sg*Pten*; blue). **C,** Representative hematoxylin and eosin (H&E) and IHC staining of a well-differentiated *MPt* EPO-GEMM (top) or *Nkx3.1*$^{CreERT2/+}$;*Pten*$^{fl/fl}$;*ARR2/Pbsn-MYC* (*NP*^{hi}*MYC*) classic GEMM prostate tumor (bottom). **D,** Representative H&E and IHC staining of a poorly differentiated *MPt* EPO-GEMM (top) or *NP*^{hi}*MYC* classic GEMM prostate tumor (bottom).

cells. The results indicated that both epithelial cell types (CK8$^+$ luminal and p63$^+$ basal cells) were targeted by prostate electroporation (Supplementary Fig. S3A). In a second experiment, a *MYC* transposon vector and the Sleeping Beauty transposase together with a sgRNA targeting *p53* (sg*p53*) were delivered into the prostate of *Probasin* (*Pb*)-*Cre4;LSL-Cas9* mice, where only luminal or basal cells expressing PB could undergo CRISPR/Cas9-mediated *p53* editing (Supplementary Fig. S3B). Following electroporation, *Pb-Cre4;LSL-Cas9* mice yielded *MP* tumors with similar DNPC histologic features and metastatic patterns as were observed in WT C57BL/6 mice (Supplementary Fig. S3C–S3E), implying that

Published OnlineFirst May 6, 2020; DOI: 10.1158/2159-8290.CD-19-1242

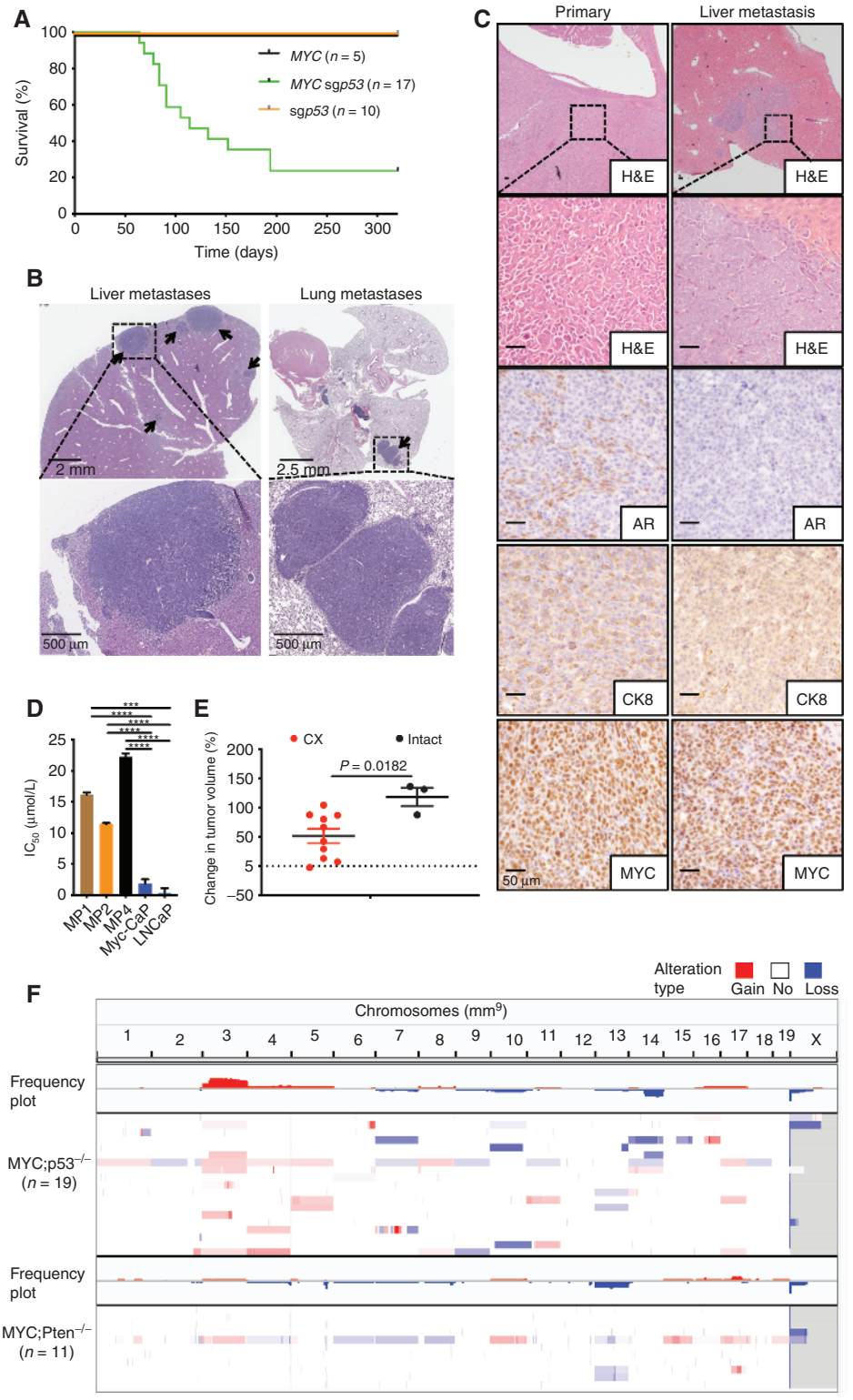

Figure 2. Engineering advanced prostate cancer *de novo* using EPO-GEMMs. **A,** Kaplan–Meier survival curve of mice electroporated with the *MYC* transposon vector and a Sleeping Beauty transposase (*MYC*; black), a CRISPR/Cas9 vector targeting *p53* (*sgp53*; orange), or all vectors (*MYC sgp53*; green). **B,** Representative H&E staining of liver and lungs isolated from mice with *MYC;sgp53* (*MP*) EPO-GEMM prostate tumors. Arrows, metastatic nodules. **C,** Representative H&E and IHC staining of a *MP* EPO-GEMM prostate tumor (left) and a corresponding liver metastasis (right). **D,** IC_{50} values for enzalutamide in indicated murine and human prostate cancer cell lines ($n = 3$; error bars, mean ± SEM; ***, $P < 0.001$; ****, $P < 0.0001$; one-way ANOVA). **E,** Change in tumor volume of *MP* EPO-GEMM prostate tumors in intact or castrated (CX) mice 1 week after surgery ($n = 3$–10; error bars, mean ± SEM; unpaired two-tailed *t* test). **F,** Frequency plot of CNV analysis of *MP* ($n = 19$) and *MPt* [$n = 11$ (from six tumors)] EPO-GEMM prostate tumors.

Published OnlineFirst May 6, 2020; DOI: 10.1158/2159-8290.CD-19-1242

prostate tumors driven by *MYC* overexpression and *p53* loss can originate from the epithelial compartment.

Human DNPC arises from prostate tumors that lose AR expression and therefore no longer display sensitivity to therapies targeting the AR signaling pathway (18, 20). Accordingly, three independent prostate cancer cell lines generated from *MP* EPO-GEMM tumors showed only a marginal reduction in growth at a 10 μmol/L therapeutic dose of the AR inhibitor enzalutamide as compared with the androgen-dependent Myc-CaP (generated from the MYC^{hi} mouse model; refs. 21, 22) and human LNCaP cell lines, which showed markedly reduced growth at lower concentrations of the drug (Fig. 2D; Supplementary Fig. S4A). Furthermore, although a modest yet statistically significant survival benefit was observed after surgical castration of a cohort of *MP* prostate tumor–bearing mice compared with the noncastrated cohort, all tumors continued to progress over a short 1-week observation period (Fig. 2E; Supplementary Fig. S4B and S4C). These data underscore the intratumoral heterogeneity of *MP* prostate tumors, with a subset of tumor cells remaining androgen-sensitive but the majority becoming resistant to androgen deprivation.

TP53-mutant human cancers often harbor complex genomes with a high rate of copy-number variations (CNV; refs. 23–25), which has been linked to metastasis formation and tumor relapse in prostate cancer (26). Similarly, murine *MP* tumors displayed a high rate of CNVs compared with *MPt* prostate tumors as assessed by sparse whole-genome sequencing (Fig. 2F). Among the gains and losses that were observed were alterations linked to late-stage disease, including recurrent amplifications in chromosome 3 (harboring *Pik3ca* and *Sox2*) and deletions in chromosome 14 (harboring the tumor suppressor *Nkx3.1*), as well as focal amplifications of *Ar* and *c-Jun* found in single tumors (Fig. 2F; Supplementary Fig. S4D–S4F; refs. 4, 5, 27, 28). Therefore, *MP* EPO-GEMM prostate tumors mirror the histologic, castration-resistant, genomic instability, and metastatic features found in human prostate cancers with *TP53* mutations.

A Subset of MYC/p53-Driven Tumors Acquire WNT Pathway Activation

To further characterize the molecular features of *MP* tumors, we transcriptionally profiled a series of samples obtained from end-stage EPO-GEMM mice. RNA-seq followed by principal component analysis (PCA) revealed that *MP* samples clustered into two distinct groups when compared with WT normal prostate or *MPt* prostate tumor samples (Fig. 3A; Supplementary Fig. S5A). GSEA as well as gene ontology pathway analysis revealed that a WNT–β-catenin pathway signature was enriched in one of the *MP* clusters (Fig. 3B; Supplementary Fig. S5B and S5C). In agreement, unsupervised clustering based on transcriptional expression of known WNT pathway genes bifurcated the *MP* samples into WNT high (WNT^{hi}) and WNT low (WNT^{lo}) groups (Fig. 3C; Supplementary Fig. S5D). Interestingly, WNT pathway activity appeared to correlate with the magnitude of metastatic spread, with WNT^{hi} tumors displaying a trend toward an overall greater frequency of metastasis, and in particular to the liver (Fig. 3D; Supplementary Fig. S5E), suggesting that deregulation of the WNT pathway may associate with prostate cancer metastasis.

Canonical WNT signaling is triggered by the binding of WNT ligands to WNT receptors such as LRP5/6, which results in the dismantling of the β-catenin destruction complex, leading to the translocation of β-catenin to the nucleus where it associates with the TCF family of transcription factors to activate WNT target genes (29). We therefore stained *MP* tumor sections for the expression of β-catenin and TCF7 as well as the presence of porcupine (PORCN), an O-Acyltransferase that is required for WNT ligand secretion and activation (30). β-catenin and TCF7 were elevated in WNT^{hi} *MP* tumors and associated with high levels of PORCN expression (Fig. 3E; Supplementary Fig. S5F and S5G). In contrast, none of these factors were detectable in WNT^{lo} *MP* tumors.

WNT^{hi} tumors also expressed other molecular features consistent with WNT pathway activation. For example, our CNV analysis indicated that two WNT^{hi} *MP* samples harbored focal amplifications of *Lrp6*, a WNT receptor, and *Wnt2b*, a WNT ligand, which were associated with significant transcriptional upregulation of these genes (Fig. 3F; Supplementary Fig. S5G–S5I). Another tumor acquired a mutation in *Apc*, a negative regulator of the WNT pathway, corresponding to an event found (albeit rarely) in human tumors (Fig. 3G). Interestingly, although *Apc* mRNA expression was reduced in both WNT^{hi} and WNT^{lo} *MP* tumors compared with normal murine prostate tissue, only WNT^{hi} tumors had induction of *Porcn* and a number of canonical WNT ligands (*Wnt 1, 2a, 2b, 10a*, and *10b*; Fig. 3C; Supplementary Fig. S5G and S5J). These data suggest that multiple factors contribute to WNT pathway activation in a subset of *MP* tumors.

WNT Pathway Alterations Are Associated with Metastatic Disease in Patients with Advanced Prostate Cancer

The link between WNT pathway activation and the more aggressive and metastatic disease identified in our EPO-GEMMs is in line with data from patients with prostate cancer (20). In a dataset of patients with either localized or advanced disease, *APC* mutations are most tightly associated with metastatic, non–castration-resistant prostate cancer (5). Further inspection of datasets of human primary [The Cancer Genome Atlas (TCGA); ref. 31] and metastatic [Stand Up To Cancer (SU2C); refs. 3, 4] prostate cancer indicated that focal amplifications of *LRP5* and *LRP6* (also observed in one of our *MP* WNT^{hi} tumors) are associated with high transcriptional LRP5 and LRP6 activity and occurred at a significantly higher rate in metastatic prostate tumors than in localized disease (Fig. 4A and B; Supplementary Fig. S6A and S6B). Although alterations in *TP53* as well as *MYC* are associated with castration-resistant disease, mutations predicted to activate WNT signaling were enriched in patients with metastatic disease independently of castration resistance status (Fig. 4C–H). Overall, patients with prostate tumors harboring WNT pathway alterations showed a significantly higher metastatic frequency and reduced overall survival (Fig. 4I and J; ref. 3). Finally, when comparing primary prostate tumor biopsies from different patient cohorts, β-catenin expression (as a readout of WNT pathway activation) was higher in tumors from patients with metastatic compared with locoregional disease (Fig. 4K and L).

Published OnlineFirst May 6, 2020; DOI: 10.1158/2159-8290.CD-19-1242

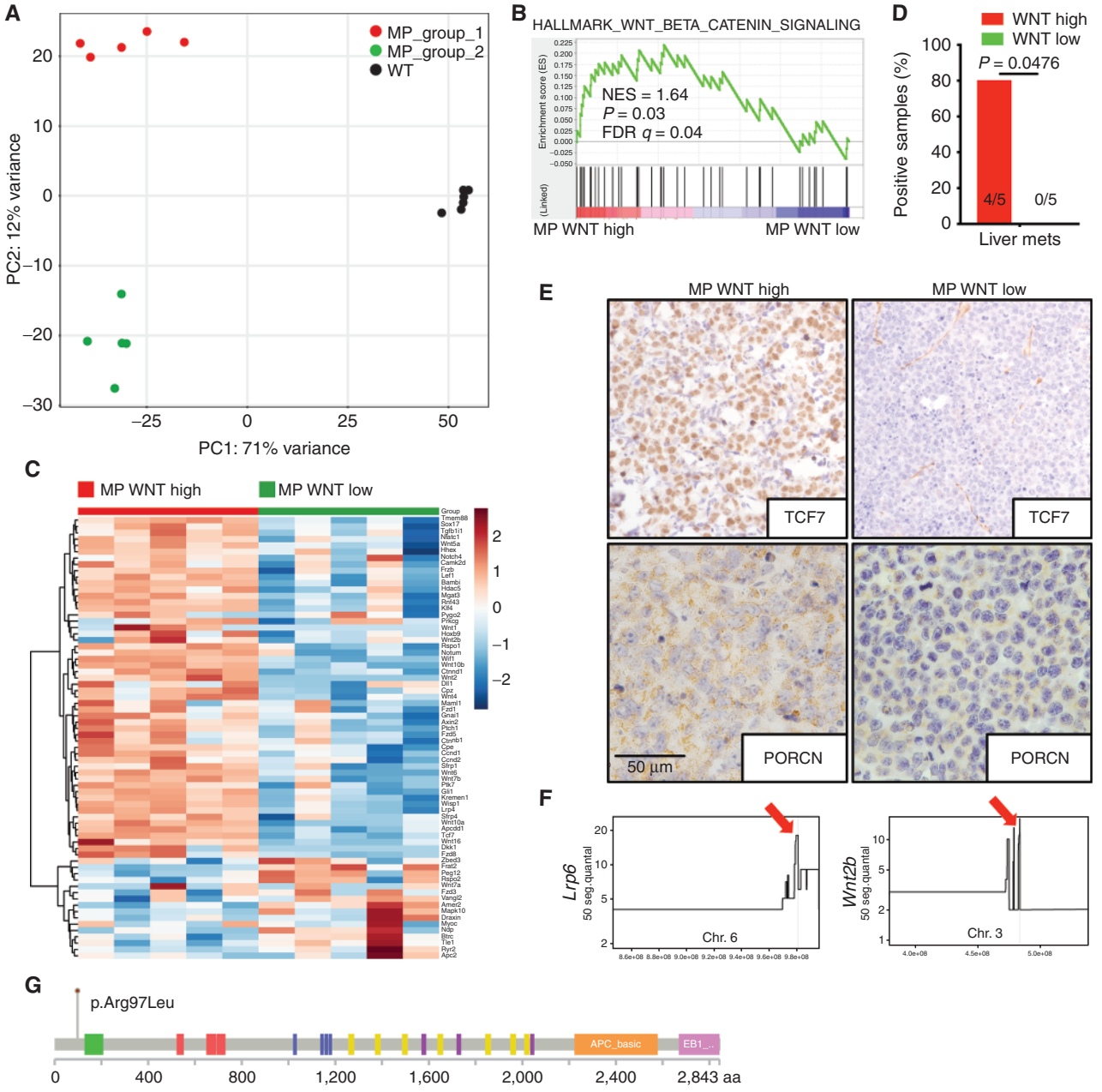

Figure 3. A subset of MYC/p53-driven tumors acquire WNT pathway activation. **A,** PCA of the transcriptional output of *MP* EPO-GEMM prostate tumors ($n = 10$) compared with WT ($n = 6$) murine prostate tissue. *MP* tumors segregate into two clusters (group 1 and group 2). **B,** GSEA of group 1 and group 2 clusters of *MP* prostate tumors from **A** reveals an enrichment for β-catenin signaling in one of the populations (hereafter *MP* WNT^{hi}). **C,** Heat map of WNT pathway gene expression in *MP* WNT^{hi} and *MP* WNT^{lo} *MP* prostate tumors ($n = 5$). **D,** Frequency of metastases in the liver in cohorts of mice with either *MP* WNT^{hi} or *MP* WNT^{lo} prostate tumors ($n = 5$; two-sided Fisher exact test). **E,** Representative IHC staining of *MP* WNT^{hi} and *MP* WNT^{lo} EPO-GEMM prostate tumors. **F,** Close-up views of clonal CNVs in WNT pathway genes *Lrp6* (left) or *Wnt2b* (right) in individual *MP* WNT^{hi} EPO-GEMM prostate tumors (see arrows). **G,** Diagram of the *Apc* gene and the position of a point mutation found in a *MP* WNT^{hi} EPO-GEMM prostate tumor.

WNT Pathway Activation Promotes Prostate Cancer Metastasis

To directly test whether WNT pathway alterations produce more aggressive and metastatic prostate cancers, we took advantage of the flexible EPO-GEMM platform to engineer tumors with constitutive WNT pathway activation. Specifically, we combined the *MYC* transposon vector with a dual CRISPR vector targeting *p53* as well as *Apc* at codon 892 (creating an N-terminal truncated protein) to generate *MPApc* EPO-GEMM mice (Supplementary Fig. S7A and S7B). As expected, the resulting tumors displayed evidence of both *p53* and *Apc* alterations, WNT pathway activation as assessed by abundant nuclear β-catenin and TCF7 expression, and all of the features of metastatic DNPC (Fig. 5A; Supplementary Fig. S7C–S7H).

Published OnlineFirst May 6, 2020; DOI: 10.1158/2159-8290.CD-19-1242

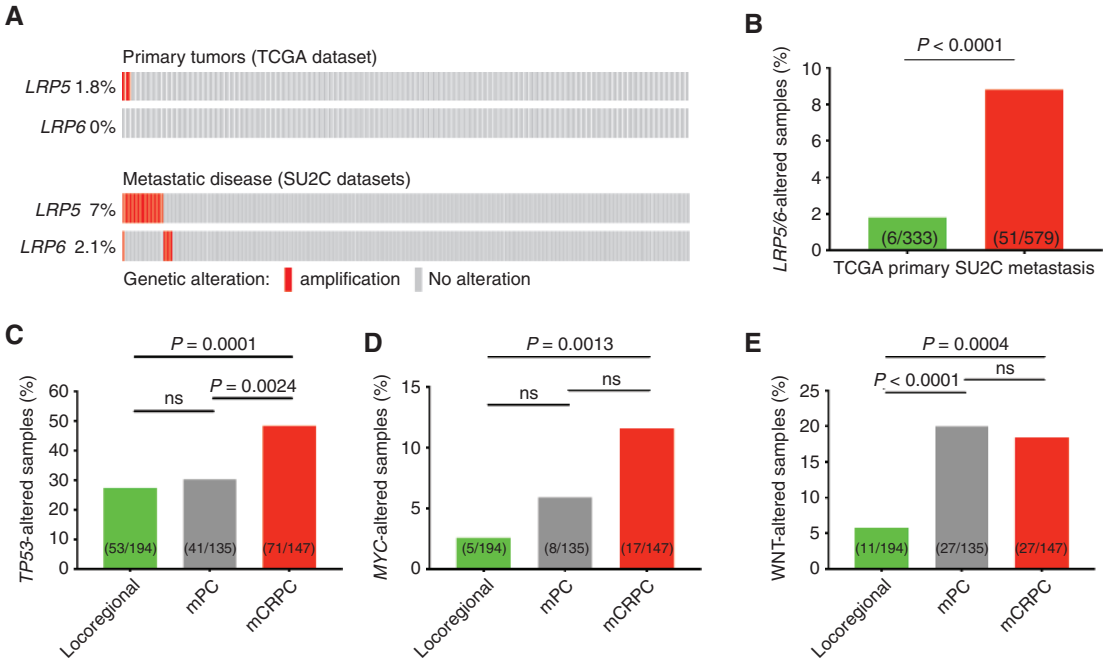

Figure 4. WNT pathway alterations are associated with metastatic disease in patients with advanced prostate cancer. **A,** OncoPrint displaying the genomic status of *LRP5* or *LRP6* in prostate cancer patient samples isolated from either primary tumors (TCGA dataset; ref. 31) or from metastatic sites (SU2C datasets; ref. 3, 4). **B,** Frequency of *LRP5* or *LRP6* amplifications in the same cohorts of patients as in **A** (two-sided Fisher exact test). **C,** Frequency of *TP53* alterations in patients with locoregional prostate cancer, metastatic but castration-sensitive prostate cancer (mPC), or mCRPC from datasets in ref. 5 (ns, not significant; two-sided Fisher exact test). **D,** Frequency of amplifications in *MYC* in the same cohorts of patients as in **C** (ns, not significant; two-sided Fisher exact test). **E,** Frequency of activating mutations in the WNT pathway genes *APC* or *CTNNB1* (encoding β-catenin) in the same cohorts of patients as in **C** (ns, not significant; two-sided Fisher exact test). (*continued on next page*)

Apc disruption also increased metastatic spread; 100% of *MPApc* mice developed distant metastases (19/19) as compared with approximately 64% of mice harboring *MP* prostate tumors (9/14; Fig. 5B and C). Furthermore, *MPApc* mice displayed a significantly reduced survival compared with *MP* cohorts (median survival 114 vs. 47 days; Fig. 5D). Moreover, the resulting *MPApc* tumors contained tumor regions with loss of E-cadherin and gain in Vimentin expression, indicative of an invasive, epithelial-to-mesenchymal transition (EMT)–like phenotype that has been previously associated with prostate cancer metastasis (Fig. 5E; ref. 32, 33). Of note, a second *Apc*-targeting sgRNA predicted to produce a more central *Apc* truncation (at codon 1529) that recapitulates the most common *Apc* mutations found in human prostate cancer (Supplementary Fig. S8A) also activated WNT signaling and produced metastatic disease in 100% of the mice (Supplementary Fig. S8B–S8E). Furthermore, EPO-GEMM models produced with *MYC, Pten*, and *Apc* alterations (at codon 892; *MPtApc*) displayed an increased frequency of metastasis compared with those with *MYC* and *Pten* alterations alone (100% vs. 54%; Fig. 5F–I; Supplementary Fig. S8F). Therefore, distinct *Apc* truncations produce WNT pathway activation and promote metastasis in prostate cancers driven by multiple genetic configurations.

Apc Mutations Drive Disease and Metastatic Progression in Prostate Cancer Organoid Models

To validate the link between WNT pathway activation and prostate cancer metastasis in a well-defined orthogonal system, we created a series of mouse prostate organoids engineered to contain different genetic alterations. Starting from either sg*p53*-edited (hereafter referred to as $p53^{-/-}$) or $Pten^{-/-}$ (derived from *Pb-Cre; Pten*$^{flox/flox}$ mice) murine organoids, we engineered WNT pathway activation by CRISPR/Cas9-mediated genome editing of the *Apc* locus (hereafter referred to as $Apc^{-/-}$). Interestingly, constitutive WNT pathway activation through *Apc* disruption (at codon 892) in combination with *Pten* or *p53* deletion led to increased organoid growth as well as changes in organoid morphology *in vitro* (Supplementary Fig. S9A–S9D).

Orthotopic transplantation of $Pten^{-/-}$;$Apc^{-/-}$ and $p53^{-/-}$;$Apc^{-/-}$ organoids into immunodeficient NOD-*scid* IL2Rγ^{null} (NSG) mice led to a higher penetrance of tumor formation and enhanced tumor growth after 15 weeks compared with organoids harboring single-gene alterations (Fig. 6A; Supplementary Fig. S9E). The resulting $p53^{-/-}$;$Apc^{-/-}$ and $Pten^{-/-}$;$Apc^{-/-}$ prostate tumors were histologically similar to *MPApc* and *MPtApc* EPO-GEMM tumors, displaying poorly differentiated tumor regions that were low for AR and the luminal markers CK8 and CK18, which was independently confirmed by immunoblotting for AR and the AR targets FKBP5 and NKX3.1 (Fig. 6B; Supplementary Fig. S9F). Phenocopying the results in the EPO-GEMMs, these $p53^{-/-}$;$Apc^{-/-}$ and $Pten^{-/-}$;$Apc^{-/-}$ tumors also displayed an EMT-like phenotype containing regions with loss of E-cadherin and gain in Vimentin expression (Fig. 6B).

Metastatic spread could not be assessed in the orthotopic transplantation model, as mice succumb to tumor-induced

Published OnlineFirst May 6, 2020; DOI: 10.1158/2159-8290.CD-19-1242

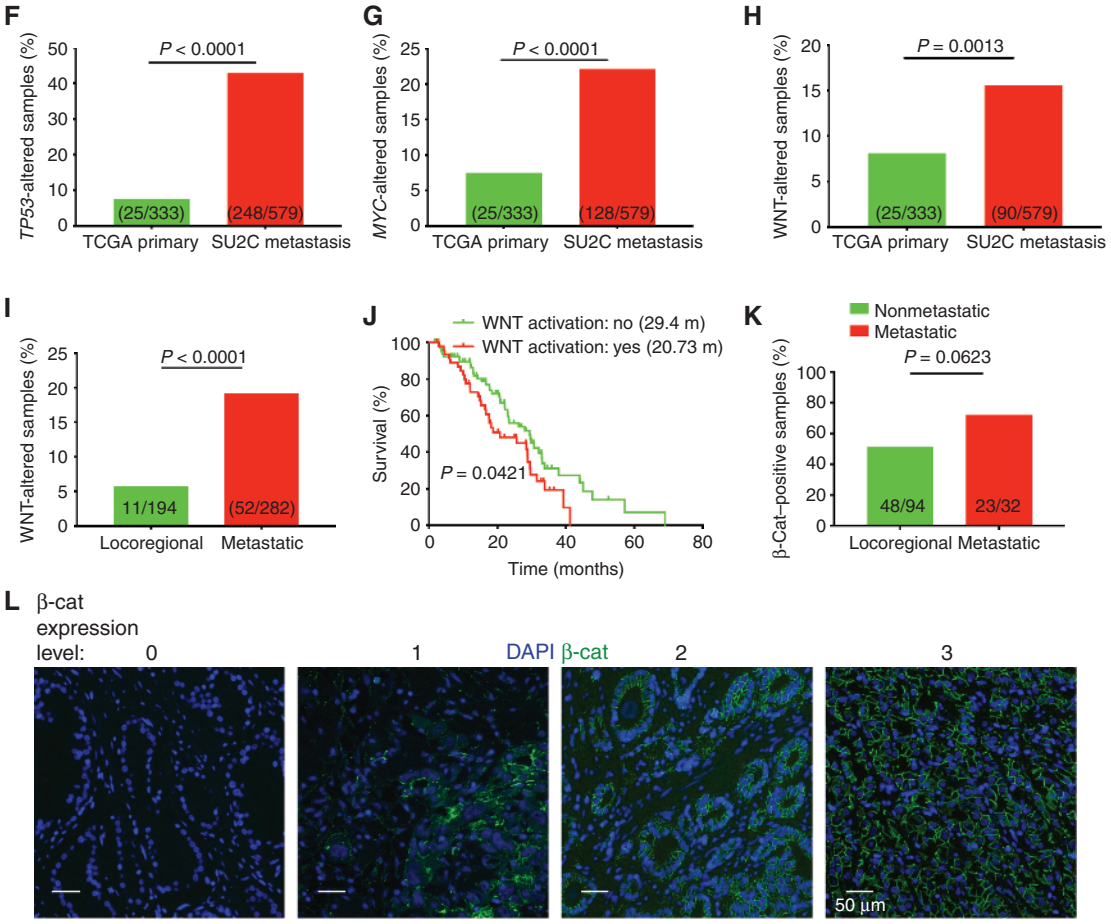

Figure 4. ***(Continued)*** **F,** Frequency of *TP53* alterations in prostate cancer patient samples isolated from either primary tumors (TCGA dataset; ref. 31) or from metastatic sites (SU2C dataset; refs. 3, 4; two-sided Fisher exact test). **G,** Frequency of amplifications in *MYC* in the same cohorts of patients as in **F** (two-sided Fisher exact test). **H,** Frequency of activating mutations in the WNT pathway genes *APC* or *CTNNB1* (encoding β-catenin) in the same cohorts of patients as in **F** (two-sided Fisher exact test). **I,** Frequency of activating mutations in the WNT pathway genes *APC* or *CTNNB1* in patients with locoregional or metastatic prostate cancer (mPC and mCRPC combined) from the same cohorts of patients as in **C** (two-sided Fisher exact test). **J,** Kaplan–Meier survival curve of patients with advanced prostate cancer with (red; $n = 47$) or without (green; $n = 81$) activating mutations in the WNT signaling pathway from the SU2C dataset (ref. 3; log-rank test). Median survival in months (m) shown in inset. **K,** Quantification of immunofluorescence staining for β-catenin in tissue microarrays (TMA) containing prostate tumor specimens from patients with locoregional or metastatic disease. The percentage of samples that stained positive for β-catenin is shown (two-sided Fisher exact test). **L,** Representative immunofluorescence staining for β-catenin (β-cat) in TMAs containing prostate tumor specimens from patients with locoregional or metastatic disease. Samples scored as 0 or 1 were considered negative, and those scored as 2 or 3 as positive for β-catenin expression.

urethral obstruction early on during tumor development. However, in a tail vein injection–based assay, prostate organoids harboring an *Apc* mutation ($p53^{-/-}$;$Apc^{-/-}$ and $Pten^{-/-}$;$Apc^{-/-}$) produced observable lung metastasis 4 weeks after injection in contrast to their corresponding $Pten^{-/-}$ or $p53^{-/-}$ controls (Fig. 6C). Similar results were obtained in $p53^{-/-}$ prostate organoids harboring a mutation in the central portion of the *Apc* gene at codon 1405 (Apc^{1405}; Supplementary Fig. S9G–S9I). The increased metastatic capacity of *Apc*-mutant tumors involved canonical WNT signaling, as short hairpin RNA (shRNA)–mediated *Ctnnb1* knockdown in organoids harboring *Apc* mutations completely ablated metastasis formation (Fig. 6D). Together, these studies validate *Apc* mutations and WNT pathway activation as a driver of disease progression, invasion, and metastasis in prostate cancer.

Targeting WNT Signaling Disrupts Prostate Cancer Metastasis

Owing to its deregulation in a plethora of other cancers (34, 35), a number of pharmacologic agents have been developed to block different components of the WNT signaling pathway. Small-molecule inhibitors of the PARP family members tankyrase 1 and 2 stabilize Axin1 and increase phosphorylation and degradation of β-catenin, and have yielded promising preclinical results (36–39). Indeed, treatment with the tankyrase inhibitor G007-LK showed markedly decreased growth in all tested prostate cancer cell lines with high WNT activity compared with those without WNT pathway induction, including normal mouse fibroblasts (Fig. 7A). Similar to results reported in a recent study exploring G007-LK efficacy in *Apc*-mutant colon cancer (39), we found that prostate tumor cells harboring

Published OnlineFirst May 6, 2020; DOI: 10.1158/2159-8290.CD-19-1242

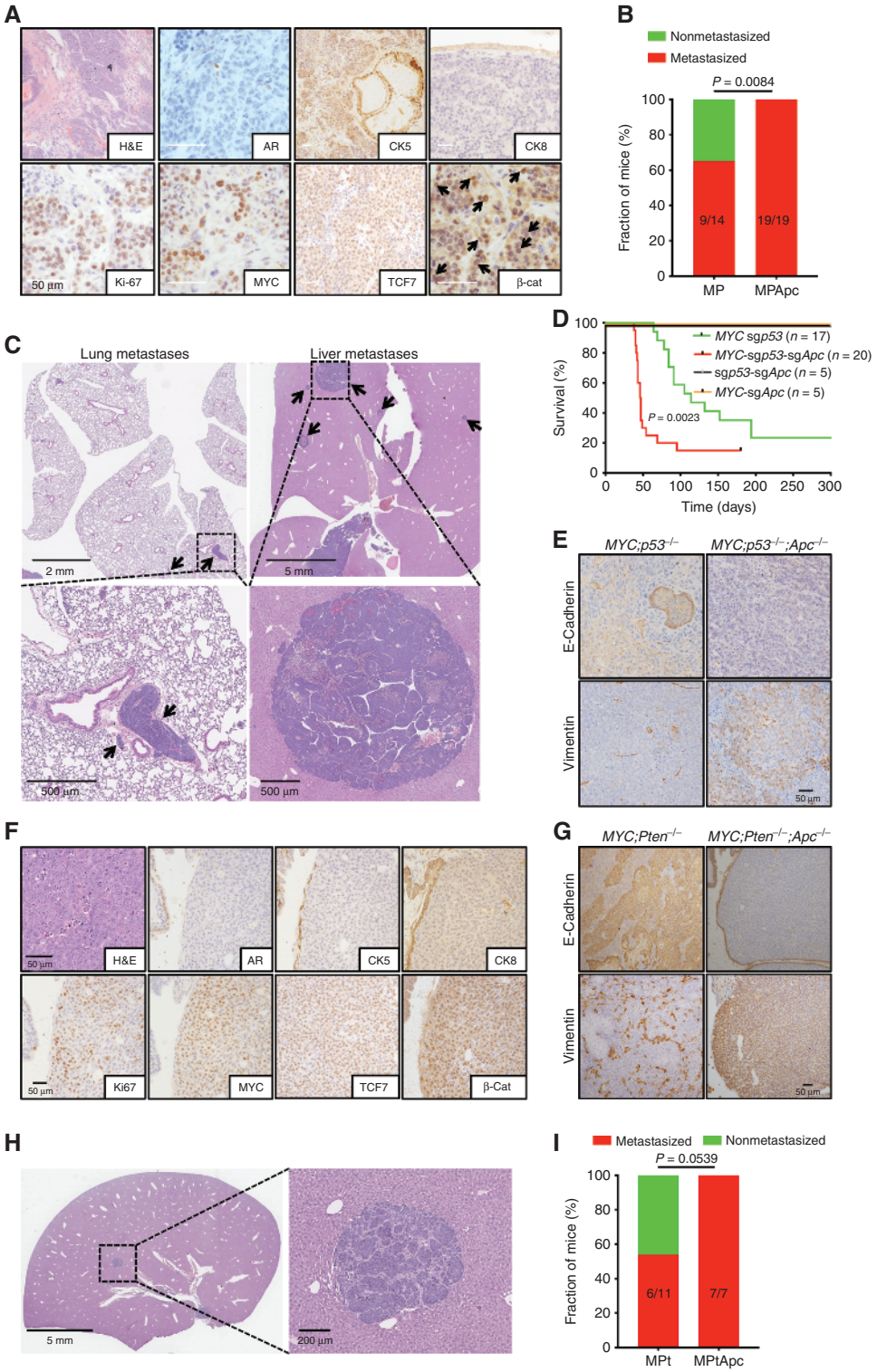

Figure 5. WNT pathway activation promotes prostate cancer metastasis. **A,** Representative H&E and IHC staining of a primary *MPApc* prostate tumor. Arrows, nuclear β-catenin (β-cat) localization. **B,** Frequency of mice with macrometastatic disease in cohorts with either *MP* or *MPApc* prostate EPO-GEMM tumors (one-sided Fisher exact test). **C,** H&E staining of liver and lung metastases isolated from mice with *MPApc* EPO-GEMM prostate tumors. Arrows, metastatic nodules. **D,** Kaplan–Meier survival curve of mice with indicated EPO-GEMM prostate tumors (log-rank test). **E,** Representative IHC staining of primary *MP* and *MPApc* EPO-GEMM prostate tumors. **F,** Representative H&E and IHC staining of a primary *MPtApc* prostate tumor. **G,** Representative IHC staining of primary *MPt* and *MPtApc* EPO-GEMM prostate tumors. **H,** H&E staining of a liver metastasis isolated from a mouse with *MPtApc* EPO-GEMM prostate tumor. **I,** Frequency of mice with macrometastatic disease in cohorts with either *MPt* or *MPtApc* prostate EPO-GEMM tumors (one-sided Fisher exact test).

Published OnlineFirst May 6, 2020; DOI: 10.1158/2159-8290.CD-19-1242

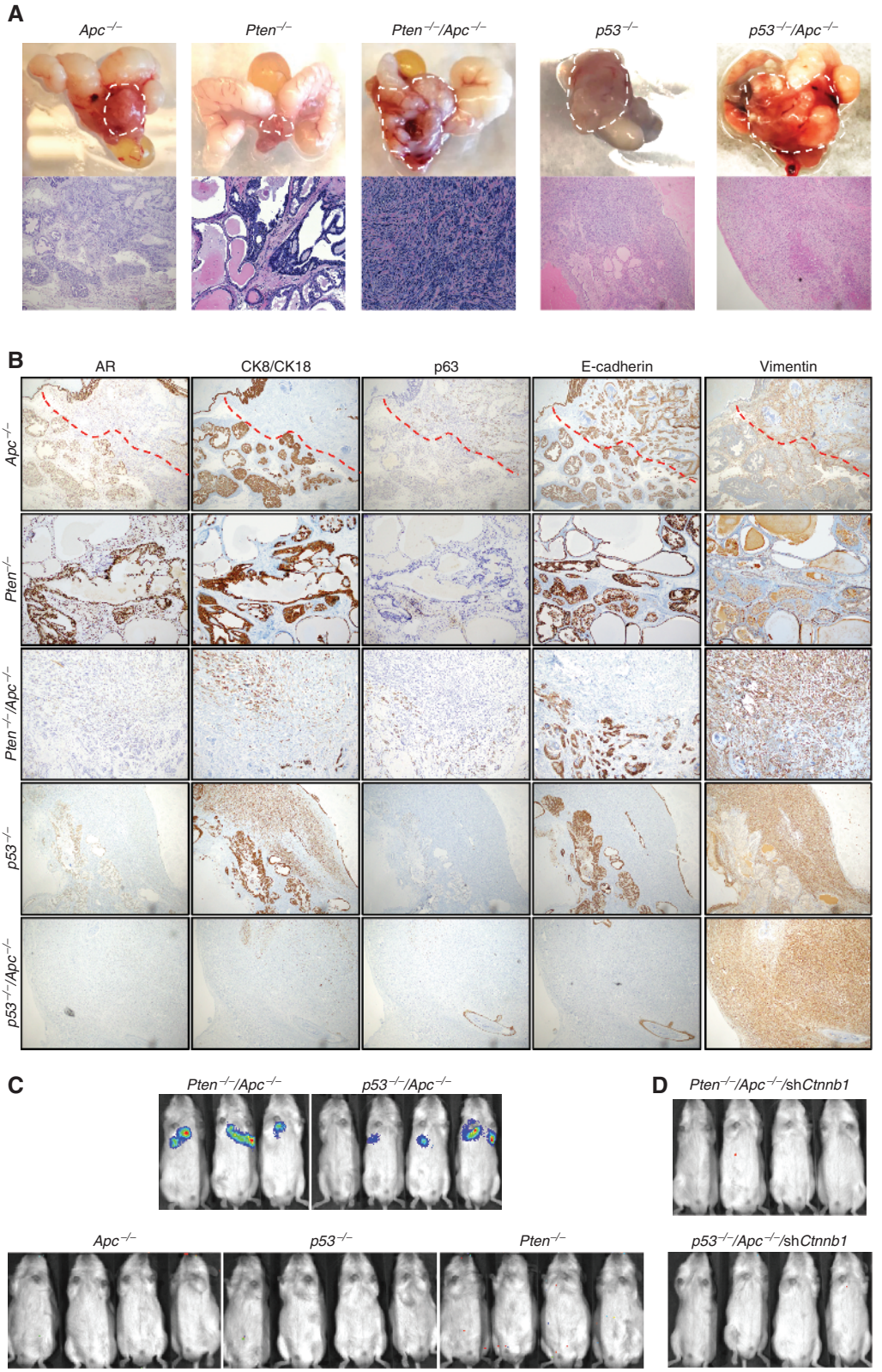

Figure 6. *Apc* mutations drive disease and metastatic progression in prostate cancer organoid models. **A,** Representative gross brightfield (top) and H&E (bottom) images of prostates of NSG mice 15 weeks after orthotopic transplantation of prostate organoids with indicated genotypes. **B,** Representative IHC staining of prostates of NSG mice 15 weeks after orthotopic transplantation of prostate organoids with indicated genotypes. **C** and **D,** Representative bioluminescence images of NSG mice 4 weeks after tail-vein injection of mouse prostate organoids with indicated genotypes ($n = 3$–4).

Published OnlineFirst May 6, 2020; DOI: 10.1158/2159-8290.CD-19-1242

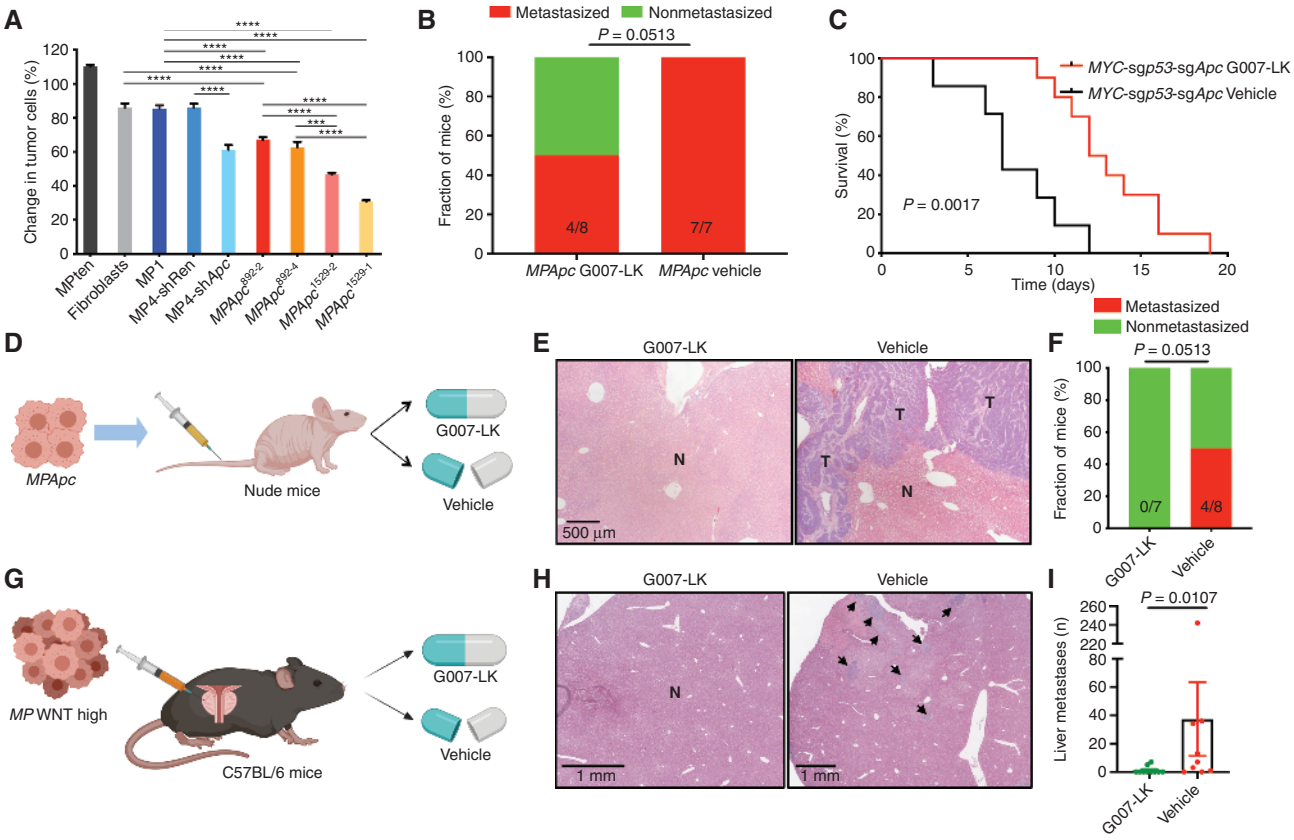

Figure 7. Targeting WNT signaling disrupts prostate cancer metastasis. **A,** Growth assay of indicated mouse prostate cancer cell lines or primary murine fibroblasts treated with 1 µmol/L of tankyrase inhibitor G007-LK for 72 hours ($n = 2$–3; error bars, mean ± SEM; one-way ANOVA). Growth is relative to treatment with vehicle control. **B,** Frequency of metastases in prostate tumor–bearing *MPApc* EPO-GEMM mice after treatment with the tankyrase inhibitor G007-LK (30 mg/kg body weight) or vehicle control (one-sided Fisher exact test). **C,** Kaplan–Meier survival curve of prostate tumor–bearing *MPApc* EPO-GEMM mice treated as in **B** (log-rank test). **D,** Schematic of *in vivo* metastasis formation assay. *MPApc* prostate cancer cell lines were tail vein–injected into *Nu/Nu* (Nude) mice and treatment with G007-LK or vehicle control was initiated one day prior to cell line injection. **E,** Representative images of H&E-stained livers isolated from mice after tail-vein injection of *MPApc* prostate cancer cell lines and treatment with G007-LK (30 mg/kg body weight) or vehicle control for 6 weeks (N, normal liver; T, tumor nodules). **F,** Frequency of liver metastases in mice after tail-vein injection of *MPApc* prostate cancer cell lines and treatment as in **E** (one-sided Fisher exact test). **G,** Schematic of orthotopic transplantation assay. *MP* WNT^{hi} prostate cancer cells harboring a WNT reporter construct (7TCF-Luciferase) were orthotopically transplanted into C57BL/6 mice. Treatment with G007-LK or vehicle control was initiated upon confirmation of tumor formation by luciferase imaging. **H,** Representative images of H&E-stained livers isolated from mice after orthotopic injection of *MP* WNT^{hi} prostate cancer cells and treatment with G007-LK (30 mg/kg body weight) or vehicle control for 4 weeks. N, normal liver; arrows, metastatic tumor nodules. **I,** Number of metastatic liver nodules in mice after orthotopic injection of *MP* WNT^{hi} prostate cancer cells and treatment as in **H** ($n = 9$–10; error bars, mean ± SEM; two-tailed Mann–Whitney test).

the central *Apc*^{1529} truncating mutation, which retains more of the β-catenin binding domain compared with the shorter N-terminal *Apc*^{892} mutant, were even more sensitive to the inhibitory effects of G007-LK treatment (Fig. 7A). The drug produced molecular changes consistent with an on-target effect, as short-term G007-LK treatment of *MPApc* prostate cancer lines led to stabilization of Axin1 and increased phosphorylation of β-catenin; it also decreased WNT activity as measured by a decrease in the mRNA levels of *Axin2*, a WNT transcriptional target, and reduced TCF7 reporter activity (Supplementary Fig. S10A–S10C). These effects could be partially rescued by overexpression of the constitutively active S45P β-catenin mutant (Supplementary Fig. S10D and S10E).

The EPO-GEMM approach makes it feasible to generate large cohorts of mice that develop relatively synchronous tumors of a defined genotype, thereby providing a powerful system to test new treatment approaches in the preclinical setting. Therefore, we generated a series of *MPApc* EPO-GEMM mice (with *Apc* truncations at codon 892) and, upon tumor manifestation as assessed by ultrasound, randomized animals and treated cohorts with vehicle or G007-LK. Tankyrase inhibition produced a significant reduction in primary tumor growth and, importantly, reduced the occurrence of macrometastatic disease (Fig. 7B; Supplementary Fig. S10F). These effects produced a near doubling in life span of G007-LK–treated prostate tumor–bearing mice as compared with those in the vehicle-treated cohort (Fig. 7C). Of note, although the reduction in metastasis observed following G007-LK treatment could arise indirectly from its inhibitory effects on primary tumor growth, G007-LK also prevented metastatic colonization in a tail vein injection assay (Fig. 7D–F).

We also produced prostate tumors in mice following orthotopic transplantation of *MPApc*^{892} cells transduced with a WNT pathway reporter construct (7TCF-luciferase) and

Published OnlineFirst May 6, 2020; DOI: 10.1158/2159-8290.CD-19-1242

initiated treatment with G007-LK or vehicle control. In both the EPO-GEMM and orthotopic transplantation setting, tankyrase inhibition significantly decreased WNT pathway transcriptional activity *in vivo* as measured by a reduction in *Axin2* mRNA levels and a decrease in 7TCF-luciferase activity following bioluminescence imaging (BLI; Supplementary Fig. S10G and S10H). In addition, none of the G007-LK–treated mice had detectable metastases at the endpoint, whereas half of the mice in the vehicle-treated cohort did (Supplementary Fig. S10I and S10J).

Finally, to rule out the possibility that the antitumor effects of tankyrase inhibition were unique to tumors with engineered WNT pathway mutations, we produced orthotopic tumors from a 7TCF-luciferase–expressing *MP* WNT^{hi} cell line and, upon tumor manifestation, mice were treated with vehicle or G007-LK (Fig. 7G). As predicted from the above findings, G007-LK treatment reduced WNT transcriptional activity (Supplementary Fig. S10K and S10L) and reduced primary tumor growth as well as the frequency and number of lung and liver metastases (Fig. 7H and I; Supplementary Fig. S10M–S10Q). Together, these data demonstrate that prostate tumors harboring WNT pathway alterations can acquire a dependency on WNT signaling that can be targeted therapeutically.

DISCUSSION

In this study we engineered and validated a nongermline GEMM (EPO-GEMM) that is flexible, efficient, and allows for the functional characterization of potential genetic drivers in prostate cancer. Although traditional prostate cancer GEMMs are extraordinarily powerful, they are time-consuming and expensive, and typically require intercrossing of several germline strains to produce tumors that arise sporadically over long time periods. In contrast, the EPO-GEMM platform allows for the production of synchronized cohorts of mice harboring genetically defined tumors at a much greater speed and scale. For example, the *Nkx3.1*$^{CreERT2/+}$;*Pten*$^{fl/fl}$;*ARR2/Pbsn-MYC* GEMM requires intercrossing of least four germline alleles, producing only a small number of animals with the correct genotype that develop tumors after a much longer latency than the *MPt* EPO-GEMM model (319 vs. 87.5 day median survival; Arriaga and colleagues, manuscript under review). Still, as with traditional GEMMs, EPO-GEMM models can recapitulate features of the human disease, and, as shown here, *MP* tumors show features of "double-negative" castration-resistant prostate cancer.

Beyond the increased speed associated with the approach, EPO-GEMMs have additional advantages compared with the traditional GEMMs. Similar to other somatic engineering approaches (40, 41), the costs of EPO-GEMM models are minimal, requiring only the purchase of as many WT mice as are needed to harbor the desired genotypes. As in human patients, tumors are focal and surrounded by normal tissue. Moreover, the models enable production of mice bearing tumors across a range of different genetic configurations in parallel, thereby facilitating their comparison. The relatively synchronous nature of tumor onset also enables the production of cohorts for preclinical studies. Tumors can also be engineered in any strain of mice, including those with alterations in particular stromal cell components, thereby enabling valuable studies of tumor–host interactions. Finally, the system is extremely portable, and in principle requires only sending plasmids and protocols to other laboratories. Some of the advantages of the EPO-GEMM system overlap with those achieved using the RapidCaP model (42), another strategy for somatic engineering of the prostate, although restrictions on the size and variety of vectors that can be used in that system limit its potential for producing genotypic diversity.

In this study, we took advantage of the unique features of the prostate EPO-GEMM approach to rapidly produce new genotypic configurations suggested from analysis of the original tumors, target different germline strains to establish the epithelial origin of the tumors, and generate synchronized cohorts of mice harboring genetically defined tumors for preclinical studies. Supporting the broad utility of this approach, others have used electroporation to produce cancers in the prostate and other organs (10–13). Other nongermline mouse modeling approaches, for example, organoid transplantation (40, 43, 44), stem cell manipulation/retransplantation (45, 46), and other somatic tissue engineering approaches (47, 48), are continuing to make mouse models more accessible to the broader research community.

Using the EPO-GEMM approach, we identified WNT pathway activation as a potent contributor to aggressive and metastatic prostate cancer. Hence, a subset of *MP* prostate tumors spontaneously acquired signatures of WNT pathway activation. These tumors showed either genetic alterations or upregulation of genes capable of activating WNT signaling. Data from genomic studies of human prostate cancer identified *APC* mutations as prominently associated with metastatic prostate cancer, and, consistent with our findings, further analyses linked previously undescribed amplifications of the WNT coreceptors *LRP5* and *LRP6* to metastatic disease in patients. Leveraging both the EPO-GEMM platform and an orthogonal organoid transplantation approach, we showed that disruption of the *Apc* tumor suppressor by modeling human-relevant mutations could drive aggressive and metastatic disease, a link that has not previously been confirmed in traditional GEMMs (49, 50). Finally, we demonstrated that a tankyrase inhibitor could repress WNT signaling, reduce metastasis, and improve overall survival.

Whereas a recent study demonstrated that *p53* loss directly leads to the secretion of WNT ligands that contribute to breast cancer metastasis by driving systemic inflammation (51), the contribution of *p53* loss and WNT pathway activation to prostate cancer progression in our model is distinct; here, *p53* loss drives progression to aggressive CRPC and, perhaps by conferring inherent genomic instability, enables the acquisition of genetic and transcriptional alterations in the WNT pathway that converge to drive metastasis. Although we did not identify a specific WNT ligand or receptor necessary for pathway activation, we found that PORCN, which is required for proper WNT ligand processing and secretion, was commonly induced only in WNT-activated tumors, suggesting that an increase in autocrine/paracrine WNT signaling is driving pathway activity. Differences in cell-of-origin may also contribute to these heterogeneous mechanisms of WNT pathway activation, as well as possibly explain why we see WNT activity in some tumors but not others.

Published OnlineFirst May 6, 2020; DOI: 10.1158/2159-8290.CD-19-1242

Importantly, alterations in *Apc* are also sufficient to promote metastasis irrespective of the *p53* (or *MYC*) genomic status, because *MPtApc* EPO-GEMMs and *Pten*$^{-/-}$;*Apc*$^{-/-}$ organoid transplant prostate tumors also displayed an increased rate of metastasis. Moreover, *Apc*-altered prostate organoids displayed enhanced metastatic progression in immunodeficient hosts, indicating that WNT pathway activation can drive metastasis formation in prostate cancer independently of its role in mediating systemic inflammation. Notably, we identified markers associated with EMT, a phenotype which has previously been linked to the acquisition of invasive and stemness characteristics and metastasis formation in prostate cancer (32, 33, 52), in tumors following WNT pathway activation, thus providing a potential mechanism of how WNT pathway activation stimulates metastatic spread. Collectively, our results functionally validate clinical associations between WNT pathway alterations, metastasis, and poor survival in patients with CRPC (ref. 3, 6; Fig. 4).

Our results also demonstrate that WNT pathway activation can confer an actionable vulnerability in the setting of mCRPC. Indeed, tumor cells harboring WNT pathway activation displayed enhanced sensitivity to tankyrase inhibition *in vitro* and *in vivo*, and our data support the notion that those tumors harboring central *Apc* truncations or alterations in WNT ligands/receptors, which are collectively the most common WNT pathway alterations found in human CRPC, will be the most sensitive to its effects. Although we cannot rule out the possibility that some of the antitumor effects produced by G007-LK result from off-target effects on stromal cells, the ability of tankyrase inhibition to impede WNT signaling in tumor cells *in vivo*, and its selective effects on WNT-altered tumor cells *in vitro*, support the notion that these effects arise, at least in part, from inhibiting WNT signaling in tumor cells themselves. Beyond this, our observation that *LRP5/6* amplifications are common in human metastatic prostate cancer raises the possibility that these tumors will also be sensitive to PORCN inhibition or other upstream WNT pathway antagonists. Although dose-limiting toxicities may preclude sufficient tankyrase inhibition in patients, our results provide proof-of-concept that WNT pathway alterations can produce actionable dependencies in prostate cancer. As therapeutic options are limited in this advanced stage of the disease, inhibition of the WNT pathway might be a valid strategy to treat patients with mCRPC.

METHODS

Cell Culture and Compounds

LNCaP and Myc-CAP cells were provided by P.A. Watson. Primary murine fibroblasts from C57BL/6 mice were purchased from Cell Biologics, Inc. and grown in complete fibroblast media (M2267). *MPt, MP,* and *MPApc* murine prostate cancer cell lines were derived from EPO-GEMM prostate tumors with these genotypes. To generate these cell lines, prostate tumors were minced, digested in DMEM media containing 3 mg/mL Dispase II (Gibco) and 1 mg/mL Collagenase IV (C5138;Sigma) for 1 hour at 37°C, and plated on 10-cm culture dishes coated with 100 μg/mL collagen (PureCol; 5005; Advanced Biomatrix). Primary cultures were passaged at least three times to remove fibroblast contamination. All prostate cancer cell lines were maintained in a humidified incubator at 37°C with 5% CO_2, and grown in RPMI1640 or DMEM supplemented with 10% FBS and 100 IU/mL penicillin/streptomycin. All cell lines used were negative for *Mycoplasma*.

Enzalutamide (S1250) and G007-LK (S7239) were purchased from Selleck Chemicals for *in vitro* studies. Drugs for *in vitro* studies were dissolved in DMSO (vehicle) to yield 10 mmol/L stock solutions and stored at −80°C. For *in vitro* studies, growth medium with or without drugs was changed every 3 days. For *in vivo* studies, G007-LK (B5830) was purchased from APExBIO. G007-LK was dissolved in 10% DMSO and then reconstituted in 20% Cremophor EL (Sigma-Aldrich) in saline.

In Vitro *Genome Editing*

For visualizing WNT pathway activity *in vitro* and *in vivo, MP* and *MPApc* cell lines were engineered to express a 7TCF-Luciferase construct (a gift from Roel Nusse, Stanford University; Addgene plasmid # 24308). Lentiviruses were packaged by cotransfection of Gag-Pol–expressing 293 T cells with expression constructs and envelope vectors (VSV-G) using the calcium phosphate method. Following transduction, cells were selected with 4 μg/mL puromycin for 1 week.

MiRE-based shRNAs targeting *Apc, Ctnnb1*, and *Renilla* were cloned into MSCV-based vectors as described previously (53, 54). Retroviruses were packaged by cotransfection of Gag-Pol–expressing 293 T cells with expression constructs and envelope vectors (VSV-G) using polyethylenimine (PEI; Sigma-Aldrich). Following transduction with shRNA retroviral constructs, cell selection was performed with 4 μg/mL puromycin for 1 week. Perturbation of WNT pathway activity following *Apc* or *Ctnnb1* knockdown was confirmed by qRT-PCR or readout of TCF activity through TOPFLASH assays.

Plasmids containing a mutant form of β-catenin (βcat^{S45P}) were provided by L.E. Dow. To engineer *MPApc* cell lines to express βcat^{S45P}, retroviruses were packaged by cotransfection of Gag-Pol–expressing 293T cells with expression constructs and envelope vectors (VSV-G) using PEI. Following transduction, cells were selected with 4 μg/mL puromycin for 1 week.

Establishment of Organoid Lines

Mouse prostate organoids were established and cultured as described previously (55). *Pten*$^{-/-}$ organoids were established from *Pb-Cre;Pten*$^{flox/flox}$ mice. WT or *Pten*$^{-/-}$ organoids were transduced with lenti-Cas9-Blast and the bulk population was selected in blasticidin for 3 days. WT organoids were then transduced with LentiCRISPRv2-sgp53 and bulk selected in puromycin for 3 days to generate p53$^{-/-}$ organoids. *Apc*-mutant organoid lines were generated using Retro-sgApc-tdTomato constructs targeting codons 884 and 1405 (provided by T. Han and L.E. Dow) and were bulk-sorted to enrich for transduced cells as described previously (56). *Ctnnb1* knockdown was achieved using MiRE-based shRNAs targeting *Ctnnb1* as described above.

In Vitro *Organoid Growth Analysis*

Organoid growth analysis was carried out as described previously (57). A thousand cells per 50 μL Matrigel dome were seeded in EGF withdrawal medium, and each timepoint consisted of three domes in a 24-well plate. Cell viability was assessed using the CellTiter-Glo Viability Assay (Promega) according to the manufacturer's protocol. All values for each timepoint were normalized to day 1 readings.

Animal Studies

All mouse experiments were approved by the Memorial Sloan Kettering Cancer Center (MSKCC; New York, NY) Internal Animal Care and Use Committee. Mice were maintained under specific pathogen-free conditions, and food and water were provided *ad libitum*. Mice were purchased from Jackson Laboratory. *Pb-Cre4* (58) male mice were crossed with *LSL-Cas9* female mice to produce *Pb-Cre4;LSL-Cas9* male mice for generation of EPO-GEMMs.

Published OnlineFirst May 6, 2020; DOI: 10.1158/2159-8290.CD-19-1242

EPO-GEMMs

Eight- to 12-week old WT C57BL/6 or transgenic *Pb-Cre;LSL-Cas9* and *Rosa26-CAGs-LSL-RIK* (59) male mice were anesthetized with isoflurane and the surgical site (pelvic region) scrubbed with a povidone-iodine scrub (Betadine) and rinsed with 70% alcohol. After opening the peritoneal cavity, the left seminal vesicle was used as a landmark and the left anterior lobe of the prostate was pulled out. Plasmid mix (50 μL; see specifications below) was injected into the left anterior lobe of the prostate using a 27.5 gauge syringe, and tweezer electrodes were tightly placed around the injection bubble. Two pulses of electrical current (60 V) given for 35-millisecond lengths at 500-millisecond intervals were then applied using an *in vivo* electroporator (Nepa Gene NEPA21 Type II Electroporator). After electroporation, the peritoneal cavity was rinsed with 0.5 mL of prewarmed saline. After the procedure, the peritoneal cavity was sutured and the skin closed with skin staples. The mice were kept at 37°C until they awoke, and postsurgery pain management was done with injections of buprenorphine and/or meloxicam for the 3 following days. Tumor formation was assessed by ultrasound imaging, and mice were sacrificed following early tumor development or at endpoint. Genome editing in EPO-GEMM tumors was confirmed by Sanger sequencing.

To generate EPO-GEMM tumors in C57BL/6 WT mice, the following vectors and concentrations were used: a pT3-MYC transposon vector (5 μg), a Sleeping Beauty transposase (SB13; 1 μg), and/or a pX330 CRISPR/Cas9 vector (20 μg; Addgene #42230) targeting the respective tumor suppressor genes. For generation of tumors in *Pb-Cre;LSL-Cas9* mice, a pT3-MYC transposon vector (10 μg; Addgene #92046), pT3-sgp53 transposon vector (20 μg), and SB13 (6 μg) were used. For assessment of tissue recombination in *Rosa26-CAGs-LSL-RIK* mice, a PGK-Cre vector (10 μg) was used. The Sleeping Beauty transposase (SB13) and the pT3 transposon vector were a generous gift from Dr. Xin Chen (University of California, San Francisco, San Francisco, CA). The pX330 vector was a gift from Feng Zhang of Broad Institute (Addgene plasmid # 42230).

The following sgRNAs were used to target the respective tumor suppressor gene locus:

Pten: GTTTGTGGTCTGCCAGCTAA
p53: ACCCTGTCACCGAGACCCC
Apc^{892}: CAGGAACCTCATCAAAACG
Apc^{1529}: CAGTTCAGGAAAACGACAA
Apc^{1405}: GTTCAGAGTGAGCCATGTAG

To generate the pX330 vector containing two sgRNAs, the vector was opened using the *Xba*I cloning site and the sgRNA-casette containing the second guide was PCR cloned into the vector using the following primers: XbaI U6 forward: ATGCTTCTAGA GAGGGCCTATTTCCCATGATT and NheI gRNA scaffold reverse: ATGTCGCTAAGCTCTAGCTCTAAAACAAAAAAGC.

Ultrasound Imaging

High-contrast ultrasound imaging was performed on a Vevo 2100 System with a MS250 13- to 24-MHz Scanhead (VisualSonics) to stage and quantify prostate tumor burden. Tumor volume was analyzed using Vevo LAB software.

BLI

BLI was used to track luciferase expression in orthotopically transplanted *MPApc* or *MP* WNT^{hi} prostate cell line tumors expressing a 7TCF-Luciferase reporter, as well as orthotopically and intravenously transplanted organoids expressing a Luciferase reporter. Mice were injected intraperitoneally with luciferin (5 mg/mouse; Gold Technologies) and then imaged on a Xenogen IVIS Spectrum Imager (PerkinElmer) 10–15 minutes later for 60 seconds. Quantification of luciferase signaling was analyzed using Living Image Software (Caliper Life Sciences).

Orthotopic Transplantation of Cell Lines

Fifty thousand *MPApc* or *MP* WNT^{hi} prostate tumor cells expressing a 7TCF-Luciferase reporter were resuspended in 25 μL of a 50% Matrigel (BD Biosciences)/50% PBS solution and injected into the right anterior prostate lobe of 8- to 10-week old male C57BL/6 mice using a Hamilton Syringe as described previously (52). BLI was used to assess tumor formation, and mice were subsequently randomized and enrolled into treatment groups. The impact on metastatic burden was assessed after 4 weeks of treatment.

In Vivo *Metastasis Assay Using Cell Lines*

Five hundred thousand *MP* or *MPApc* prostate tumor cells were resuspended in 400 μL of PBS and tail vein injected into 8- to 10-week-old *Nu/Nu* (Nude) male mice.

Orthotopic Transplantation of Organoids

A LentiLuciferase-Neo construct was transduced into all organoid lines and bulk selected for 3 days in neomycin. 3×10^6 cells per mouse were used for orthotopic injection. Organoids were dissociated into single cells and resuspended in 50% Matrigel and 50% medium before injection into male NSG mice. *In vivo* luciferase signals were measured once a week on an IVIS spectrum imager. Mouse prostate tissues were collected after 13 weeks for histologic analysis.

In Vivo *Metastasis Assay Using Organoids*

Twenty-five thousand dissociated LentiLuciferase-Neo transduced organoid cells were resuspended in 400 μL of PBS and tail vein injected into NSG mice. *In vivo* luciferase signals were measured once a week on an IVIS spectrum imager. Mouse lung tissues were collected 40 days after injection.

Surgical Castration

Castration was performed as described previously (60). EPO-GEMM mice were monitored for prostate tumor development by ultrasound, and enrolled and randomized into treatment groups once tumors reached 500 mm^3. Ultrasound imaging was repeated every week following castration to assess changes in prostate tumor burden. Upon sacrifice, prostate tumor tissue was allocated for 10% formalin fixation and Optimal cutting temperature frozen blocks.

Preclinical Treatment Studies

EPO-GEMM mice were monitored for prostate tumor development by ultrasound, and enrolled and randomized into treatment groups once tumors reached 500 mm^3. C57BL/6 mice orthotopically transplanted with *MP* and *MPApc* prostate tumors cells expressing a 7TCF-Luciferase reporter were evaluated by BLI to verify tumor development before being randomized into various study cohorts. Nude mice tail vein injected with *MPApc* prostate tumor cells were randomized and treated with either G007-LK or vehicle control the day before injection to assess metastasis prevention.

Mice were treated with vehicle or G007-LK (30 mg/kg body weight) by intraperitoneal injection for 5 consecutive days followed by 2 days off treatment. Ultrasound and/or BLI were repeated every week during treatment to assess changes in prostate tumor burden. No obvious toxicities were observed in vehicle- or drug-treated animals as assessed by changes in body weight. Upon sacrifice, prostate tumor tissue was allocated for 10% formalin fixation and snap-frozen tissue for DNA/RNA analysis.

Analysis of Metastasis Burden

The presence of peritoneal, lymph node, thorax, lung, and liver metastases was determined at survival or experimental endpoint by gross examination under a dissecting scope. Metastasis burden and

Published OnlineFirst May 6, 2020; DOI: 10.1158/2159-8290.CD-19-1242

the total number of individual metastases was further quantified from hematoxylin and eosin (H&E)–stained sections. The presence of DTCs in the bone marrow of EPO-GEMM mice was assessed following PCR genotyping for the presence of the human *MYC* allele in the bone marrow flushes from the hind limbs of these mice. PCR genotyping of *MP* EPO-GEMM prostate tumors and normal WT prostate tissue was used as positive and negative controls, respectively.

IHC and Immunofluorescence

Tissues were fixed overnight in 10% formalin, embedded in paraffin, and cut into 5-μm sections. H&E and IHC/immunofluorescence staining was performed using standard protocols. The following primary antibodies were used: AR (Sc-816), p63 (Sc-8431), and CK8 (Sc-8020; Santa Cruz Biotechnology); Porcupine (PORCN; AB105543), MYC (AB32072), Ki-67 (AB16667), and LRP6 (AB24386; Abcam); Cytokeratin 5 (CK5; 905501) and Cytokeratin 8 (CK8; 904801; BioLegend); β-catenin (BD610153), E-cadherin (BD610181), and ASCL1 (MASH1;BD556604; BD Biosciences); Synaptophysin (SYP; 1485-1; Epitomics); mKate2 (AB233; Evrogen); p63 (4A4, Ventana); Vimentin (5741), and TCF1/TCF7 (2203; Cell Signaling Technology). Histopathologic features in EPO-GEMM primary prostate tumors and metastases were assessed by a trained veterinary pathologist (J.E. Wilkinson).

High-Throughput RNA-seq

For RNA-seq analysis of the transcriptional profiles of *MPt* and *MP* EPO-GEMM prostate tumors, as well as normal anterior lobe tissue from prostates of WT C57BL/6, total RNA was extracted from bulk tissue using the RNeasy Mini Kit (Qiagen). Purified polyA mRNA was subsequently fragmented, and first- and second-strand cDNA synthesis was performed using standard Illumina mRNA TruSeq library preparation protocols. Double-stranded cDNA was subsequently processed for TruSeq dual-index Illumina library generation. For sequencing, pooled multiplexed libraries were run on a HiSeq 2500 machine on RAPID mode. Approximately 10×10^6 76-bp single-end reads were retrieved per replicate condition. Resulting RNA-seq data were analyzed by removing adaptor sequences using Trimmomatic (61), aligning sequencing data to GRCm38.91(mm10) with STAR (62), and genome wide transcript counting using featureCounts (63) to generate a TPM matrix of transcript counts. Genes were identified as differentially expressed using R package DESeq2 with a cutoff of absolute $\log_2$FoldChange ≥ 1 and $P_{adj} < 0.05$ between experimental conditions (64). Functional enrichments of these differentially expressed genes were performed with enrichment analysis tool Enrichr (65) and the retrieved combined score [log(*P* value) × *z*-score) was displayed.

Clustering and GSEA

PCA was performed using the DESeq2 package in R. Gene expressions of RNA-seq data were clustered using hierarchical clustering based on one minus Pearson correlation test. For pathway enrichment analysis, the weighted GSEA Preranked mode was used on a set of curated signatures in the molecular signatures database (MSigDB v7.0; http://www.broadinstitute.org/gsea/msigdb/index.jsp). From 22,596 signatures, only signatures with 15–500 genes were considered for further analyses. From the results, enriched signatures with a P_{adj} value less than 0.05 were considered as statistically significant.

CNVs

CNVs were inferred from sparse whole-genome sequencing data as described previously (66, 67). In brief, 1 μg of bulk genomic DNA was extracted from prostate tumors and tissue using the DNeasy Blood and Tissue Kit (Qiagen) and sonicated using the Covaris instrument. Sonicated DNA was subsequently end-repaired/A-tailed, followed by ligation of TruSeq dual indexed adaptors. Indexed libraries were enriched via PCR and sequenced in multiplex fashion using the Illumina HiSeq2500 Instrument to achieve roughly 1×10^6 uniquely mappable reads per sample, a read count sufficient to allow copy-number inference to a resolution of approximately 400 kb. For data analysis, uniquely mapped reads were counted in genomic bins corrected for mappability. Read counts were subsequently corrected for guanine cytosine content, normalized, and segmented using circular binary segmentation. Segmented copy-number calls are illustrated as relative gains and losses to the median copy number of the entire genome. Broad events (chromosome wide and several megabase sized events) are discernible in a genome-wide manner as illustrated in Fig. 2F. Focal events, namely chromosomal amplifications, are discernible in zoom-in views of chromosomes as depicted in Fig. 3F; Supplementary Fig. S4D and S4E.

Mouse MSK-IMPACT

Tumors were profiled for genomic alterations in M-IMPACT_v1key cancer-associated genes using our custom, deep sequencing MSK-IMPACT assay that surveys 468 known cancer driver genes. Custom DNA probes were designed for targeted sequencing of all exons and selected introns of oncogenes, tumor suppressor genes, and members of pathways deemed actionable by targeted therapies. Genomic DNA from tumor and matched normal WT prostate anterior lobe tissue samples were subjected to sequence library preparation and exon capture (NimbleGen). Up to 30 barcoded sequence libraries were pooled at equimolar concentrations and input into a single exon capture reaction, as described previously (68). Pooled libraries containing captured DNA fragments were subsequently sequenced on the Illumina HiSeq System.

Sequence data were demultiplexed using BCL2FASTQv1.8.3 (Illumina), and vesitigial adapter sequences were removed from the 3′ end of sequence reads. Reads were aligned in paired-end mode to the hg19 b37 version of the genome using BWA-MEM (Burrows-Wheeler Alignment tool). Local realignment and quality score recalibration were performed using Genome Analysis Toolkit (GATK) according to GATK best practices (69). Paired-sample variant calling was performed on tumor samples and their respective matched normals to identify point mutations/single-nucleotide variants (SNV) and small insertions/deletion (indel). MuTect (version 1.1.4; ref. 70) was used for SNV calling and SomaticIndelDetector, a tool in GATKv.2.3.9, was used for detecting indel events. Variants were subsequently annotated using Annovar, and annotations relative to the canonical transcript for each gene (derived from a list of known canonical transcripts obtained from the UCSC genome browser) were reported.

Tissue Microarray

Tissue microarrays (purchased from US Biolab) containing a total of 126 prostate tumor specimens from 66 patients with localized and metastatic disease were stained for β-catenin expression by immunofluorescence through the Molecular Cytology Core Facility at MSKCC using a Discovery XT Processor (Ventana Medical Systems). Briefly, tissue sections were deparaffinized with EZPrep Buffer (Ventana Medical Systems) and antigen retrieval was performed with CC1 Buffer (Ventana Medical Systems). Sections were blocked for 30 minutes with Background Buster Solution (Innovex), followed by avidin-biotin blocking for 8 minutes (Ventana Medical Systems). Sections were incubated with a β-catenin antibody (8814; Cell Signaling Technology) for 5 hours, followed by a 60-minute incubation with biotinylated goat anti-rabbit IgG (PK6101; Vector Laboratories) at a 1:200 dilution. Detection was performed with Streptavidin-HRP D (part of DABMap Kit, Ventana Medical Systems), followed by incubation with Tyramide Alexa 488 (B40953;

Published OnlineFirst May 6, 2020; DOI: 10.1158/2159-8290.CD-19-1242

Invitrogen) prepared according to the manufacturer's instructions. After staining, slides were counterstained with DAPI (D9542; Sigma Aldrich) for 10 minutes and cover slipped with Mowiol. Tissues were then scored on a 0–3 scale for β-catenin expression, with scores of 0 and 1 as "negative" and 2 and 3 as "positive" for β-catenin.

Human Clinical Data Analysis

CBioPortal.org was used to plot the frequency of mutations, amplifications, and/or deletions in genes of interest in patients with prostate cancer from various datasets. *TP53* alterations included deep deletions (homozygous loss) as well as missense, inframe, and truncating mutations. A Kaplan–Meier survival curve of patients with prostate cancer with or without WNT pathway alterations was generated using part of the SU2C dataset (3), which included 47 patients in the WNT-activated group and 81 patients in the non–WNT activated group. Patients were randomized into the two groups based on WNT pathway activating alterations in the following genes: *CTNNB1, APC, AXIN2, WIF1, SFRP1, DKK1, RNF43, ZNRF3, GSK3B, TCF7, TLE1, LRP5, LRP6*, and *WNT2B* (71). The percentage of WNT pathway–altered prostate tumor specimens from patients with locoregional versus metastatic disease was determined from an MSK-IMPACT dataset (5), which included 194 patients with locoregional prostate cancer, 135 patients with metastatic prostate cancer, and 147 patients with mCRPC. Locoregional disease in this setting indicated disease without distant clinical or pathologic spread, including lymph node involvement in the pelvis only. *LRP5* and *LRP6* amplification frequency was determined from a dataset containing samples obtained from primary tumors where CNV analysis was performed by Affymetrix SNP 6.0 (31), or two datasets containing samples obtained from metastatic sites where CNV analysis was performed by whole-exome sequencing (3, 4). *LRP5* and *LRP6* expression levels in amplified (AMP or GAIN) or nonamplified tumors were determined in mCRPC patients samples from the SU2C dataset (3) using normalized fpkm values and CNV calls.

Patients and Samples

Histopathologic analysis was performed on a primary prostate tumor tissue biopsy from a patient with mCRPC treated at MSKCC harboring a *MYC* amplification and p53 alteration (L114Ffs*33) as part of the MSK-IMPACT cohort (5, 72). Clinical sequencing analysis (MSK-IMPACT) was completed on this and other samples and collected using a web-based electronic data capture. IHC and sequencing analysis on human tissue samples was performed under MSKCC Institutional Review Board approval. All samples and clinical data were deidentified.

AR$^+$, NE$^+$, and DNPC Classification

We adhered to the AR$^+$/neuroendocrine-positive (NE$^+$)/DN prostate cancer subtype classification as proposed in ref. 18. Briefly, AR and neuroendocrine scores were calculated according to the expression of the mRNA *z*-scores of 10 AR activity genes (*KLK3, KLK2, TMPRSS2, FKBP5, NKX3-1, PLPP1, PMEPA1, PART1, ALDH1A3*, and *STEAP4*) and 10 neuroendocrine signature genes (*SYP, CHGA, CHGB, ENO2, CHRNB2, SCG3, SCN3A, PCSK1, ELAVL4*, and *NKX2-1*) for mouse and human prostate samples (19). Subsequently, samples for each dataset were normalized from 1 (highest expression of either neuroendocrine or AR score, respectively) to 0 (lowest expression of either neuroendocrine or AR score, respectively) as displayed in the scattered plot. IHC staining and quantification of AR and SYP/ASCL1 (neuroendocrine) marker expression was also used for subtype classification in some mouse and human tumors. DNPCs were defined as those that lacked expression of both AR$^+$ and NE$^+$ markers.

TOPFLASH Assay

Ten thousand cells were plated in 100 μL of media containing 10% FBS per well of a black-walled 96-well plate (Perkin Elmer). After 24 hours, cells were transfected using PEI with 170 ng of TOPFLASH Firefly reporter and 30 ng of pRL-SV40P *Renilla* constructs provided by T. Tamella (MSKCC). In initial experiments, the WNT-insensitive FOPFLASH Firefly reporter (also provided by T. Tamella) was used to rule out signal background (not shown). Thirty-six hours after transfection, *Firefly* and *Renilla* signals were detected using Dual-Glo Luciferase Detection Reagents (Promega) according to the manufacturer's instructions. A Varioskan Flash Plate Reader (Thermo Fischer Scientific) was used to detect luminescence. To control for transfection efficiency, *Firefly* luciferase levels were normalized to *Renilla* luciferase levels to generate the measure of relative 7TCF activity.

Immunoblotting

Cell lysis was performed using RIPA Buffer (Cell signaling Technology) supplemented with phosphatase inhibitors (5 mmol/L sodium fluoride, 1 mmol/L sodium orthovanadate, 1 mmol/L sodium pyrophosphate, and 1 mmol/L β-glycerophosphate) and protease inhibitors (Protease Inhibitor Cocktail Tablets, Roche). Protein concentration was determined using a Bradford Protein Assay Kit (Bio-Rad). Proteins were separated by SDS-PAGE and transferred to polyvinyl difluoride membranes (Millipore) according to the standard protocols. Membranes were immunoblotted with antibodies against Axin1 (2087), phospho-β-catenin S33/S37/T41 (9561), PTEN (9188), P53 (2524), and FKBP5 (12210) from Cell Signaling Technology, AR (ab108341), cyclophilin B (ab16045), and NKX3.1 (ab196020) from Abcam, APC (OP44) from Millipore, and p21 (sc-6246) from Santa Cruz Biotechnology in 5% BSA in TBS-blocking buffer. After primary antibody incubation, membranes were probed with an electrochemiluminescence anti-rabbit IgG or anti-mouse IgG secondary antibody (1:10,000) from GE Healthcare Life Science and imaged using a FluorChem M system (Protein Simple). Protein loading was measured using a monoclonal β-actin antibody directly conjugated to horseradish peroxidase (1:20,000) from Sigma-Aldrich and imaged as above.

qRT-PCR

Total RNA was isolated using the RNeasy Mini Kit (Qiagen), and cDNA was obtained using the TaqMan Reverse Transcription Reagents (Applied Biosystems). Real-time PCR was performed in triplicate using SYBR Green PCR Master Mix (Applied Biosystems) on the ViiA 7 Real-Time PCR System (Invitrogen). GAPDH and mRn18s served as endogenous normalization controls.

Cell Viability Assay

Five thousand cells were plated in 100 μL of media containing 10% FBS per well of a black-walled 96-well plate (Perkin Elmer). The next day, the media were changed and cells were treated with G007-LK or enzalutamide for 72 hours. Following treatment, cell viability was assessed using the CellTiter-Glo Viability Assay (Promega) according to the manufacturer's protocol. IC_{50} calculations were made using Prism 6 Software (GraphPad Software).

Statistical Analysis

Statistical analyses were performed as described in the figure legend for each experiment. Group size was determined on the basis of the results of preliminary experiments, and no statistical method was used to predetermine sample size. The indicated sample size (*n*) represents biological replicates. Group allocation and outcome assessment were not performed in a blinded manner. All samples that met proper experimental conditions were included in the analysis. Survival was measured using the Kaplan–Meier method. Statistical significance was determined by one- and two-way ANOVA, Fisher exact test, Student *t* test, log-rank test, Mann–Whitney test, and Pearson correlation using Prism 6 Software (GraphPad Software) as indicated. Significance was set at $P < 0.05$.

Published OnlineFirst May 6, 2020; DOI: 10.1158/2159-8290.CD-19-1242

Data Availability

RNA-seq data generated in this study are deposited in the Gene Expression Omnibus database under accession number GSE139340. Mouse IMPACT sequencing data presented in this study are deposited in the NCBI BioProject database under accession number PRJNA610252.

Figure Preparation

Figures were prepared using BioRender.com for scientific illustrations and Illustrator CC 2020 (Adobe).

Disclosure of Potential Conflicts of Interest

L.E. Dow is a scientific advisor at Mirimus Inc. C.L Sawyers is member of the board of directors at Novartis and a member of the scientific advisory board at ORIC, Arsenal, Column Group, Nextech, Agios, Beigene, Blueprint, Housey, KSQ, PMV, Petra, and Foghorn, has ownership interest in enzalutamide royalties and apalutamide royalties, and is a Cold Spring Harbor Laboratories Science Trustee. S.W. Lowe is a founder and SAB member at Oric Pharmaceuticals. No potential conflicts of interest were disclosed by the other authors.

Authors' Contributions

Conception and design: J. Leibold, M. Ruscetti, Z. Cao, C.L. Sawyers, S.W. Lowe

Development of methodology: J. Leibold, M. Ruscetti, Z. Cao, F.J. Sánchez-Rivera, P.A. Watson

Acquisition of data (provided animals, acquired and managed patients, provided facilities, etc.): J. Leibold, M. Ruscetti, Z. Cao, T. Baslan, M. Zou, W. Abida, T. Han, K.M. Tsanov, L. Zamechek, A. Kulick, C. Amor, S. Tian, K. Rybczyk, N.R. Salgado, E. de Stanchina, J.E. Wilkinson, C. Abate-Shen

Analysis and interpretation of data (e.g., statistical analysis, biostatistics, computational analysis): J. Leibold, M. Ruscetti, Z. Cao, Y.-J. Ho, T. Baslan, W. Abida, J. Feucht, K.M. Tsanov, A. Kulick, C. Amor, K. Rybczyk, J.E. Wilkinson, L.E. Dow, C. Abate-Shen

Writing, review, and/or revision of the manuscript: J. Leibold, M. Ruscetti, Z. Cao, Y.-J. Ho, W. Abida, F.M. Barriga, N.R. Salgado, L.E. Dow, C. Abate-Shen, C.L. Sawyers, S.W. Lowe

Administrative, technical, or material support (i.e., reporting or organizing data, constructing databases): J. Leibold, M. Ruscetti, Z. Cao, L. Zamechek, K. Rybczyk

Study supervision: L.E. Dow, C. Abate-Shen, C.L. Sawyers, S.W. Lowe

Acknowledgments

We thank T. Tammela and O. Grbovic-Huezo for sharing tissue samples; E.M. Schatoff for sharing reagents, plasmids, and experimental protocols; N. Socci and the Bioinformatics Core for assistance with Mouse IMPACT sequencing analysis; F. Sanchez-Vega and N. Schultz for assistance with genomic analysis of human datasets; A. Tehuitzil, A. Wuest, A. Kim, C.J. Hagen, D. Choi, A.C. Agudelo Rivera, and A. Gaglio for technical assistance; C.J. Sherr and H. Wu for helpful comments on the manuscript; and other members of the Lowe laboratory for insightful discussions. We thank William H. and Alice Goodwin and the Commonwealth Foundation for Cancer Research for research support. This work was also supported by a P50 CA092629 Prostate Cancer Spore grant (to S.W. Lowe), a Memorial Sloan Kettering Cancer Center Support grant (P30 CA008748), NIH grants (R01 CA155169, CA193837, CA224079, CA092629, and CA160001 to C.L. Sawyers; CA233944 and CA087497 to S.W. Lowe; U54 OD020355 to S.W. Lowe and E. de Stanchina; and R01 CA183929 and CA173481 to C. Abate-Shen), Starr Cancer Consortium grants I10-0062 and I12-0007 (to C.L. Sawyers), and an Agilent Thought Leader Award (to S.W. Lowe). S.W. Lowe is the Geoffrey Beene Chair for Cancer Biology and S.W. Lowe and C.L. Sawyers are investigators at the Howard Hughes Medical Institute (HHMI). We also acknowledge support to J. Leibold from the German Research Foundation (DFG) and the Shulamit Katzman Endowed Postdoctoral Research Fellowship, to M. Ruscetti from the American Cancer Society (PF-16-115-01-TBG) and the NCI (K99 CA241110), to T. Baslan from the William C. and Joyce C. O'Neil Charitable Trust and Memorial Sloan Kettering Single Cell Sequencing Initiative, to J. Feucht from the Care-for-Rare Foundation and the German Research Foundation (DFG), to C. Amor from La Caixa foundation and a Harold E. Varmus graduate student fellowship from the Gerstner Sloan Kettering graduate school, to F.M. Barriga from a GMTEC Postdoctoral Research Fellowship and a MSKCC TROT Postdoctoral Fellowship (NIH T32CA160001), to K.M. Tsanov from The Jane Coffin Childs Memorial Fund for Medical Research, and to F.J. Sánchez-Rivera from HHMI (Hanna Gray Fellowship).

Received October 22, 2019; revised March 26, 2020; accepted May 1, 2020; published first May 6, 2020.

REFERENCES

1. Siegel RL, Miller KD, Jemal A. Cancer statistics, 2018. CA Cancer J Clin 2018;68:7–30.
2. Huggins C. Control of cancers of man by endocrinologic methods. Cancer Res 1957;17:467–72.
3. Abida W, Cyrta J, Heller G, Prandi D, Armenia J, Coleman I, et al. Genomic correlates of clinical outcome in advanced prostate cancer. Proc Natl Acad Sci U S A 2019;116:11428–36.
4. Robinson D, Van Allen EM, Wu YM, Schultz N, Lonigro RJ, Mosquera JM, et al. Integrative clinical genomics of advanced prostate cancer. Cell 2015;162:454.
5. Abida W, Armenia J, Gopalan A, Brennan R, Walsh M, Barron D, et al. Prospective genomic profiling of prostate cancer across disease states reveals germline and somatic alterations that may affect clinical decision making. JCO Precis Oncol 2017;2017.
6. Armenia J, Wankowicz SAM, Liu D, Gao J, Kundra R, Reznik E, et al. The long tail of oncogenic drivers in prostate cancer. Nat Genet 2018;50:645–51.
7. Sun Y, Campisi J, Higano C, Beer TM, Porter P, Coleman I, et al. Treatment-induced damage to the tumor microenvironment promotes prostate cancer therapy resistance through WNT16B. Nat Med 2012;18:1359–68.
8. Gurel B, Iwata T, Koh CM, Jenkins RB, Lan F, Van Dang C, et al. Nuclear MYC protein overexpression is an early alteration in human prostate carcinogenesis. Mod Pathol 2008;21:1156–67.
9. Arriaga JM, Abate-Shen C. Genetically engineered mouse models of prostate cancer in the postgenomic era. Cold Spring Harb Perspect Med 2019;9:pii:a030528.
10. Choi HJ, Lee HB, Jung S, Park HK, Jo W, Cho SM, et al. Development of a mouse model of prostate cancer using the sleeping beauty transposon and electroporation. Molecules 2018;23:pii:E1360.
11. Maresch R, Mueller S, Veltkamp C, Ollinger R, Friedrich M, Heid I, et al. Multiplexed pancreatic genome engineering and cancer induction by transfection-based CRISPR/Cas9 delivery in mice. Nat Commun 2016;7:10770.
12. Park JS, Lim KM, Park SG, Jung SY, Choi HJ, Lee DH, et al. Pancreatic cancer induced by in vivo electroporation-enhanced sleeping beauty transposon gene delivery system in mouse. Pancreas 2014;43:614–8.
13. Seehawer M, Heinzmann F, D'Artista L, Harbig J, Roux PF, Hoenicke L, et al. Necroptosis microenvironment directs lineage commitment in liver cancer. Nature 2018;562:69–75.
14. Hubbard GK, Mutton LN, Khalili M, McMullin RP, Hicks JL, Bianchi-Frias D, et al. Combined MYC activation and Pten loss are sufficient to create genomic instability and lethal metastatic prostate cancer. Cancer Res 2016;76:283–92.

Published OnlineFirst May 6, 2020; DOI: 10.1158/2159-8290.CD-19-1242

15. Kim J, Eltoum IE, Roh M, Wang J, Abdulkadir SA. Interactions between cells with distinct mutations in c-MYC and Pten in prostate cancer. PLoS Genet 2009;5:e1000542.
16. Grasso CS, Wu YM, Robinson DR, Cao X, Dhanasekaran SM, Khan AP, et al. The mutational landscape of lethal castration-resistant prostate cancer. Nature 2012;487:239–43.
17. De Laere B, Oeyen S, Mayrhofer M, Whitington T, van Dam PJ, Van Oyen P, et al. TP53 outperforms other androgen receptor biomarkers to predict abiraterone or enzalutamide outcome in metastatic castration-resistant prostate cancer. Clin Cancer Res 2019;25:1766–73.
18. Bluemn EG, Coleman IM, Lucas JM, Coleman RT, Hernandez-Lopez S, Tharakan R, et al. Androgen receptor pathway-independent prostate cancer is sustained through FGF signaling. Cancer Cell 2017;32:474–89.
19. Kumar A, Coleman I, Morrissey C, Zhang X, True LD, Gulati R, et al. Substantial interindividual and limited intraindividual genomic diversity among tumors from men with metastatic prostate cancer. Nat Med 2016;22:369–78.
20. Chen WS, Aggarwal R, Zhang L, Zhao SG, Thomas GV, Beer TM, et al. Genomic drivers of poor prognosis and enzalutamide resistance in metastatic castration-resistant prostate cancer. Eur Urol 2019;76:562–71.
21. Watson PA, Ellwood-Yen K, King JC, Wongvipat J, Lebeau MM, Sawyers CL. Context-dependent hormone-refractory progression revealed through characterization of a novel murine prostate cancer cell line. Cancer Res 2005;65:11565–71.
22. Ellwood-Yen K, Graeber TG, Wongvipat J, Iruela-Arispe ML, Zhang J, Matusik R, et al. Myc-driven murine prostate cancer shares molecular features with human prostate tumors. Cancer Cell 2003;4:223–38.
23. Shlien A, Tabori U, Marshall CR, Pienkowska M, Feuk L, Novokmet A, et al. Excessive genomic DNA copy number variation in the Li-Fraumeni cancer predisposition syndrome. Proc Natl Acad Sci U S A 2008;105:11264–9.
24. Ciriello G, Miller ML, Aksoy BA, Senbabaoglu Y, Schultz N, Sander C. Emerging landscape of oncogenic signatures across human cancers. Nat Genet 2013;45:1127–33.
25. Quigley DA, Dang HX, Zhao SG, Lloyd P, Aggarwal R, Alumkal JJ, et al. Genomic hallmarks and structural variation in metastatic prostate cancer. Cell 2018;174:758–69.
26. Hieronymus H, Schultz N, Gopalan A, Carver BS, Chang MT, Xiao Y, et al. Copy number alteration burden predicts prostate cancer relapse. Proc Natl Acad Sci U S A 2014;111:11139–44.
27. Ouyang X, Jessen WJ, Al-Ahmadie H, Serio AM, Lin Y, Shih WJ, et al. Activator protein-1 transcription factors are associated with progression and recurrence of prostate cancer. Cancer Res 2008;68:2132–44.
28. Visakorpi T, Hyytinen E, Koivisto P, Tanner M, Keinanen R, Palmberg C, et al. In vivo amplification of the androgen receptor gene and progression of human prostate cancer. Nat Genet 1995;9:401–6.
29. Logan CY, Nusse R. The Wnt signaling pathway in development and disease. Annu Rev Cell Dev Biol 2004;20:781–810.
30. Hausmann G, Banziger C, Basler K. Helping wingless take flight: how WNT proteins are secreted. Nat Rev Mol Cell Biol 2007;8:331–6.
31. Cancer Genome Atlas Research Network. The molecular taxonomy of primary prostate cancer. Cell 2015;163:1011–25.
32. Montanari M, Rossetti S, Cavaliere C, D'Aniello C, Malzone MG, Vanacore D, et al. Epithelial-mesenchymal transition in prostate cancer: an overview. Oncotarget 2017;8:35376–89.
33. Stylianou N, Lehman ML, Wang C, Fard AT, Rockstroh A, Fazli L, et al. A molecular portrait of epithelial-mesenchymal plasticity in prostate cancer associated with clinical outcome. Oncogene 2019;38:913–34.
34. Reya T, Clevers H. Wnt signalling in stem cells and cancer. Nature 2005;434:843–50.
35. Barker N, Clevers H. Mining the Wnt pathway for cancer therapeutics. Nat Rev Drug Discov 2006;5:997–1014.
36. Huang SM, Mishina YM, Liu S, Cheung A, Stegmeier F, Michaud GA, et al. Tankyrase inhibition stabilizes axin and antagonizes Wnt signalling. Nature 2009;461:614–20.
37. Ferri M, Liscio P, Carotti A, Asciutti S, Sardella R, Macchiarulo A, et al. Targeting Wnt-driven cancers: discovery of novel tankyrase inhibitors. Eur J Med Chem 2017;142:506–22.
38. Waaler J, Machon O, Tumova L, Dinh H, Korinek V, Wilson SR, et al. A novel tankyrase inhibitor decreases canonical Wnt signaling in colon carcinoma cells and reduces tumor growth in conditional APC mutant mice. Cancer Res 2012;72:2822–32.
39. Schatoff EM, Goswami S, Zafra MP, Foronda M, Shusterman M, Leach BI, et al. Distinct colorectal cancer-associated APC mutations dictate response to tankyrase inhibition. Cancer Discov 2019;9:1358–71.
40. Roper J, Tammela T, Cetinbas NM, Akkad A, Roghanian A, Rickelt S, et al. In vivo genome editing and organoid transplantation models of colorectal cancer and metastasis. Nat Biotechnol 2017;35:569–76.
41. Sanchez-Rivera FJ, Papagiannakopoulos T, Romero R, Tammela T, Bauer MR, Bhutkar A, et al. Rapid modelling of cooperating genetic events in cancer through somatic genome editing. Nature 2014;516:428–31.
42. Cho H, Herzka T, Zheng W, Qi J, Wilkinson JE, Bradner JE, et al. RapidCaP, a novel GEM model for metastatic prostate cancer analysis and therapy, reveals myc as a driver of Pten-mutant metastasis. Cancer Discov 2014;4:318–33.
43. O'Rourke KP, Loizou E, Livshits G, Schatoff EM, Baslan T, Manchado E, et al. Transplantation of engineered organoids enables rapid generation of metastatic mouse models of colorectal cancer. Nat Biotechnol 2017;35:577–82.
44. Boj SF, Hwang CI, Baker LA, Chio II, Engle DD, Corbo V, et al. Organoid models of human and mouse ductal pancreatic cancer. Cell 2015;160:324–38.
45. Saborowski M, Saborowski A, Morris JPt, Bosbach B, Dow LE, Pelletier J, et al. A modular and flexible ESC-based mouse model of pancreatic cancer. Genes Dev 2014;28:85–97.
46. Zuber J, Radtke I, Pardee TS, Zhao Z, Rappaport AR, Luo W, et al. Mouse models of human AML accurately predict chemotherapy response. Genes Dev 2009;23:877–89.
47. Kang TW, Yevsa T, Woller N, Hoenicke L, Wuestefeld T, Dauch D, et al. Senescence surveillance of pre-malignant hepatocytes limits liver cancer development. Nature 2011;479:547–51.
48. Hickman MA, Malone RW, Lehmann-Bruinsma K, Sih TR, Knoell D, Szoka FC, et al. Gene expression following direct injection of DNA into liver. Hum Gene Ther 1994;5:1477–83.
49. Jefferies MT, Cox AC, Shorning BY, Meniel V, Griffiths D, Kynaston HG, et al. PTEN loss and activation of K-RAS and β-catenin cooperate to accelerate prostate tumourigenesis. J Pathol 2017;243:442–56.
50. Lee SH, Luong R, Johnson DT, Cunha GR, Rivina L, Gonzalgo ML, et al. Androgen signaling is a confounding factor for β-catenin-mediated prostate tumorigenesis. Oncogene 2016;35:702–14.
51. Wellenstein MD, Coffelt SB, Duits DEM, van Miltenburg MH, Slagter M, de Rink I, et al. Loss of p53 triggers WNT-dependent systemic inflammation to drive breast cancer metastasis. Nature 2019; 572:538–42.
52. Ruscetti M, Quach B, Dadashian EL, Mulholland DJ, Wu H. Tracking and functional characterization of epithelial-mesenchymal transition and mesenchymal tumor cells during prostate cancer metastasis. Cancer Res 2015;75:2749–59.
53. Chicas A, Wang X, Zhang C, McCurrach M, Zhao Z, Mert O, et al. Dissecting the unique role of the retinoblastoma tumor suppressor during cellular senescence. Cancer Cell 2010;17:376–87.
54. Chien Y, Scuoppo C, Wang X, Fang X, Balgley B, Bolden JE, et al. Control of the senescence-associated secretory phenotype by NF-κB promotes senescence and enhances chemosensitivity. Genes Dev 2011; 25:2125–36.
55. Drost J, Karthaus WR, Gao D, Driehuis E, Sawyers CL, Chen Y, et al. Organoid culture systems for prostate epithelial and cancer tissue. Nat Protoc 2016;11:347–58.
56. Schatoff EM, Zafra MP, Dow LE. Base editing the mammalian genome. Methods 2019;164–5:100–8.
57. Adams EJ, Karthaus WR, Hoover E, Liu D, Gruet A, Zhang Z, et al. FOXA1 mutations alter pioneering activity, differentiation and prostate cancer phenotypes. Nature 2019;571:408–12.
58. Wu X, Wu J, Huang J, Powell WC, Zhang J, Matusik RJ, et al. Generation of a prostate epithelial cell-specific Cre transgenic mouse model for tissue-specific gene ablation. Mech Dev 2001;101:61–9.

Published OnlineFirst May 6, 2020; DOI: 10.1158/2159-8290.CD-19-1242

59. Dow LE, Nasr Z, Saborowski M, Ebbesen SH, Manchado E, Tasdemir N, et al. Conditional reverse tet-transactivator mouse strains for the efficient induction of TRE-regulated transgenes in mice. PLoS One 2014;9:e95236.
60. Ruscetti M, Dadashian EL, Guo W, Quach B, Mulholland DJ, Park JW, et al. HDAC inhibition impedes epithelial-mesenchymal plasticity and suppresses metastatic, castration-resistant prostate cancer. Oncogene 2016;35:3781–95.
61. Bolger AM, Lohse M, Usadel B. Trimmomatic: a flexible trimmer for Illumina sequence data. Bioinformatics 2014;30:2114–20.
62. Dobin A, Davis CA, Schlesinger F, Drenkow J, Zaleski C, Jha S, et al. STAR: ultrafast universal RNA-seq aligner. Bioinformatics 2013;29:15–21.
63. Anders S, Pyl PT, Huber W. HTSeq–a Python framework to work with high-throughput sequencing data. Bioinformatics 2015;31:166–9.
64. Love MI, Huber W, Anders S. Moderated estimation of fold change and dispersion for RNA-seq data with DESeq2. Genome Biol 2014;15:550.
65. Kuleshov MV, Jones MR, Rouillard AD, Fernandez NF, Duan Q, Wang Z, et al. Enrichr: a comprehensive gene set enrichment analysis web server 2016 update. Nucleic Acids Res 2016;44:W90–7.
66. Baslan T, Kendall J, Rodgers L, Cox H, Riggs M, Stepansky A, et al. Genome-wide copy number analysis of single cells. Nat Protoc 2012;7:1024–41.
67. Baslan T, Kendall J, Ward B, Cox H, Leotta A, Rodgers L, et al. Optimizing sparse sequencing of single cells for highly multiplex copy number profiling. Genome Res 2015;25:714–24.
68. Won HH, Scott SN, Brannon AR, Shah RH, Berger MF. Detecting somatic genetic alterations in tumor specimens by exon capture and massively parallel sequencing. J Vis Exp 2013:e50710.
69. DePristo MA, Banks E, Poplin R, Garimella KV, Maguire JR, Hartl C, et al. A framework for variation discovery and genotyping using next-generation DNA sequencing data. Nat Genet 2011;43:491–8.
70. Cibulskis K, Lawrence MS, Carter SL, Sivachenko A, Jaffe D, Sougnez C, et al. Sensitive detection of somatic point mutations in impure and heterogeneous cancer samples. Nat Biotechnol 2013;31:213–9.
71. Sanchez-Vega F, Mina M, Armenia J, Chatila WK, Luna A, La KC, et al. Oncogenic signaling pathways in The Cancer Genome Atlas. Cell 2018;173:321–37.
72. Zehir A, Benayed R, Shah RH, Syed A, Middha S, Kim HR, et al. Mutational landscape of metastatic cancer revealed from prospective clinical sequencing of 10,000 patients. Nat Med 2017;23:703–13.

AACR American Association for Cancer Research

CANCER DISCOVERY

Somatic Tissue Engineering in Mouse Models Reveals an Actionable Role for WNT Pathway Alterations in Prostate Cancer Metastasis

Josef Leibold, Marcus Ruscetti, Zhen Cao, et al.

Cancer Discov 2020;10:1038-1057. Published OnlineFirst May 6, 2020.